R. & M. No. 3635

MINISTRY OF TECHNOLOGY

AERONAUTICAL RESEARCH COUNCIL
REPORTS AND MEMORANDA

Experiments with Biconvex and Double-Wedge Aerofoils in Low-Density, Supersonic Flow

By E. W. E. ROGERS and C. J. BERRY
Aerodynamics Division N.P.L.

LONDON: HER MAJESTY'S STATIONERY OFFICE
1970
PRICE £1 4*s* 0*d* [£1·20] NET

Experiments with Biconvex and Double-Wedge Aerofoils in Low-Density, Supersonic Flow

By E. W. E. ROGERS and C. J. BERRY
Aerodynamics Division N.P.L.

Reports and Memoranda No. 3635*
November, 1968

Summary.

This report contains an analysis of the surface-pressure distributions on two aerofoil sections of 10% thickness/chord ratio, at Mach numbers near 2 and 4, and at Reynolds numbers between 93 and 1920, based on model chord. It is shown that with the exception of those hole positions within the upstream influence of the trailing-edge, all surface pressures over a wide range of incidence may be correlated using a viscous-interaction parameter $\bar{\chi}$, in a manner similar to that for the flat plate at zero incidence. For the front surfaces of the double-wedge aerofoil, the local inviscid flow conditions near these surfaces represent those of the equivalent free stream where these are used in formulating the appropriate value of χ. For the rear wedge surfaces, and for the biconvex surfaces, correlation is achieved if it is assumed that the equivalent local flow only attains some fraction (about 0·6) of the surface expansion from the shoulder or the leading edge respectively. This reduction of the expansion angle is due to the presence of a very thick laminar boundary layer in the expansion region. A simple theoretical model is developed which provides an estimate of the effect.

The pressure distributions have been integrated to give section lift and pressure-drag. The lift-curve slope is significantly higher than that predicted by inviscid theory due to the viscous-induced pressure increments. These also increase the pressure-drag so that the ratio of lift to pressure-drag is close to that measured elsewhere at high Reynolds numbers (around 6×10^5). The addition of skin-friction drag to the low-Reynolds-number data increases the section drag considerably and quite high incidences are needed before the lift/drag ratio exceeds unity.

LIST OF CONTENTS

1. *Introduction.*

The flow about slender bodies immersed in low-Reynolds-number continuum or transitional flow is dominated by the thick laminar boundary layers which develop on the body surfaces. The displacement effect of these boundary layers modifies the surface pressure distribution and hence affects the overall aerodynamic characteristics of the body. The magnitude of such viscous-induced effects has been studied for a number of years, with perhaps most attention being given to simple geometric shapes like the flat plate and the cone. A measure of understanding has indeed been attained of the way in which the hypersonic viscous-interaction parameter $M^3 \sqrt{C}/\sqrt{Re} = \bar{\chi}$ (where M is a Mach number, Re a Reynolds number characterising the flow, and C is the Chapman-Rubesin factor) can be used to correlate surface pressures and heat-transfer rates (*see* Refs. 8a to 8d for example). There is still room for argument about the extent of the flow zones dominated by weak and strong interactions, and, more recently, about the effect of merging between the boundary layer and the adjacent shock wave.

It is also apparent that the basic displacement effect associated with boundary-layer growth from a leading edge may be modified when sudden changes in surface geometry occur; these changes may be associated with a shoulder or with the trailing edge, and the resulting interaction effects can then spread well upstream and downstream from the disturbing influence. The magnitude of such effects, important in practical aerodynamic problems, is not easy to estimate however and there is a clear need for more experimental data. Information is also lacking on the aerodynamic behaviour of lifting surfaces in low-Reynolds-number flow, assessed in terms of viscous-interaction phenomena.

The NPL research programme on low-density aerodynamics is primarily concerned with the influence of viscosity on flows about wings and bodies, and hence with the characteristics and structure of the thick laminar boundary layer. Early work investigated flows about cones[1] and cylinders[2]; later lifting plates and delta wings[3], trailing-edge flaps[4] and steps[5] were tested and reported upon. Between October and December 1965 the surface pressures were measured on two aerofoils of biconvex and double-wedge section at stream Mach numbers near 2 and 4, but no analysis of the data was then attempted. It was felt, however, that the results were of sufficient interest to justify detailed consideration, even after this lapse of time.

2. *Experimental Details.*

2.1. *The Tunnel.*

The NPL low-density tunnel and its operation, as employed for the tests described in the present report*, are described in some detail in Ref. 1. Two axisymmetric nozzles, providing open-jet test sections, were then available, designed for nominal Mach numbers near 2 and 4. Data were obtained at three working-section pressure levels (p_∞) for each nozzle; because the boundary-layer growth on the nozzle wall varies with p_∞, the actual test Mach number (M_∞) changes too. Calibration of the flow at the model position[1] showed that, for a given value of p_∞, M_∞ did not alter significantly within the isentropic core in either the streamwise or cross-stream direction. The following relationships between test Mach number and static pressure, measured in millitorrs were used in the data analysis:

*Subsequent modifications include the provision of an additional oil-diffusion pump, the use of a diffuser and a stagnation-chamber heater, and the development of more complicated instrumentation. The tunnel Mach number range has been increased considerably.

TABLE 1

$< p_\infty >$ Newtons/sq.m	$< p_\infty >$ (millitorrs)	M_∞	$Re_{\infty,c}$	$\bar{\chi}_\infty = \frac{M_\infty^3\sqrt{C}}{\sqrt{Re_{\infty,c}}}$
4·4	33	1·79	93	0·59
6·9	52	2·09	204	0·63
8·6	64·5	2·12	254	0·60
4·4	33	3·95	790	2·19
6·0	45	4·04	1170	1·93
8·7	65	4·19	1920	1·68

The stagnation temperature of the flow in all cases was nearly atmospheric and has been taken as 288°K. The Reynolds number ($Re_{\infty,c}$), based on the stream conditions and model chord, varies between 93 at $M_\infty = 1{\cdot}79$ and 1920 at $M_\infty = 4{\cdot}19$. It is convenient to use the viscous interaction parameter $\bar{\chi}_\infty$ as a measure of induced-pressure effects; this quantity is also listed in Table 1.

2.2. *The Models.*

The symmetrical biconvex and double-wedge aerofoil sections used in the present tests provide very suitable test surfaces for studying low-density, viscous flows. The overall aerodynamic behaviour of these sections over a range of incidence (α) provides useful information on the magnitude of the viscous influence on simple aerofoil shapes; the inviscid flow is simple and well-defined. Moreover, there are two conditions for which the viscous effects are of particular interest: a uniform expansion and a sudden expansion. These two conditions are provided by the biconvex and double-wedge profiles respectively.

The two profiles, whose thickness/chord ratio is 0·1, are shown in Fig. 1*. For defining the surface pressure distribution each section had 10 pressure holes, of diameter 0·010 in (0·25 mm) placed on one surface only at the stations indicated in Fig. 1. The aerofoil chord was 1·0 in (2·54 cm) and the model span (5 in; 12·7 cm) was sufficiently long to allow it to extend completely across the jet issuing from the nozzle. The pressure holes were placed near mid-span but in an irregular pattern to avoid local contamination effects. The usable core of uniform flow is much smaller than the actual jet; the diameter of this core varies with Mach number and static pressure[1] between about 1·5 in (3·8 cm) and 3·2 in (8·1 cm). Care was taken to ensure that the pressure-plotting section of the aerofoils was always immersed in this uniform region.

The leading-edge radius of each section was about 0·0015 in (0·04 mm) and this is sufficiently small to allow bluntness effects to be neglected (*see* Ref. 7).

2.3. *Test Procedure.*

The NPL low-density tunnel runs continuously, and after an initial warming-up period the test flow is stable. For the pressure levels and stream Mach numbers listed in Table 1 the aerofoil surface pressures were measured using the standard thermistor manometer (*see* Appendix of Ref. 1); for pressure levels between 5μ and 400μ (where μ is a convenient symbol for a millitorr) roughly the range of the present

*Note that the hole distributions in terms of x/c for the two sections are not always similar. This arises because for reasons irrelevant to the present text, the leading edge was defined differently on each profile at each nominal Mach number.

surface-pressure measurements, the accuracy is better than $\pm 0{\cdot}5\mu$. Calibration of the thermistor manometer, using a McLeod gauge, was carried out at frequent intervals throughout the investigation.

The aerofoil models have no internal cooling and all measurements were therefore obtained under zero heat-transfer conditions.

A remotely-controlled incidence gear mounted in the tunnel, but outside the test jet, allowed pressure measurements to be obtained at incidences up to $\pm 50°$; at incidences above about $\pm 20°$, however, the increased model blockage caused significant changes in the test flow, and as a consequence data for very high incidences have not been used in the present report.

Because the surface holes used to define the local pressure distribution are all on one surface, it is convenient to regard this surface as the upper one, and to define positive and negative incidences accordingly. Thus a positive incidence leads in general to surface pressures below those appropriate to zero incidence, and a negative incidence to increased pressures.

3. *Analysis of Surface Pressures.*

3.1. *General Characteristics.*

The distribution of upper-surface pressures for the two aerofoils at $M_\infty = 4{\cdot}04$, $p_\infty = 45\mu$, over a wide range of incidence is shown in Figs. 2a and b; p_L is the measured local pressure. The rapidly-growing boundary layer over the model surface is responsible for the pressure gradient that exists on both the forward and rearward surfaces of the double-wedge section. For the biconvex aerofoil the inviscid pressure falls almost linearly along the surface; viscous-interaction enhances this gradient and makes it non-uniform. At a lower stream Mach number (2·09) very similar results are obtained and these are shown in Figs. 3a and b. At this condition the trailing-edge interaction becomes rather more pronounced, and is well illustrated, for example, on the biconvex section at $\alpha = +20°$; the local pressure reaches a minimum near $x/c = 0{\cdot}7$ and thereafter rises slightly towards the higher pressure-levels of the wake region.

The effect of changing stream static pressure (and to some extent test Mach number) is illustrated in Figs. 4a and b, and for comparison the inviscid pressure distribution at $M_\infty = 4$ has been added. Near the leading edge of the double-wedge aerofoil the actual pressures recorded are around three times those predicted in the absence of boundary-layer effects. The largest viscous-interaction effect occurs at the lowest stream pressure and highest value of $\bar{\chi}_\infty$.

Near $M_\infty = 2$ a marked coupling between p_∞ and M_∞ occurs and this makes the interpretation of the changes in local pressure level with these quantities more difficult (Figs. 5a and b). Indeed in assessing the significance and magnitude of the viscous-induced pressure changes, some general correlation of the surface pressure is required. This is attempted in the following Sections.

3.2. *Double-Wedge Section; Forward-Facing Surfaces.*

Perhaps the simplest type of flow field is that associated with the forward-facing surfaces of the double-wedge aerofoil. The pressures recorded from the front five holes ($0{\cdot}05 \leqslant x/c \leqslant 0{\cdot}45$) at $M_\infty = 4{\cdot}04$ can be correlated very simply in terms of the parameter $\bar{\chi}_0$ where the relevant distance is now that between the leading edge and the pressure hole (x) (Fig. 6). For all incidences the pressure ratio p_L/p_∞ varies linearly with $\bar{\chi}_0$, though the hole nearest the shoulder shows some influence of the expansion just downstream. The results for $\alpha = 0°$ have been extended by including corresponding data for all three static pressure levels, and the correlation is quite satisfactory. Similar agreement exists at all other incidences.

The measured pressures at holes 6 to 10 ($0{\cdot}5 \leqslant x/c \leqslant 0{\cdot}9$) have been included on this Figure for $\alpha = 0°$ as solid symbols to show that downstream of the expansion some alternative method of correlation is needed if such data are to be brought into line with those from the forward-facing surfaces. This aspect is discussed later in Section 3.3.

In Fig. 6 the effect of the aerofoil incidence is most marked, but it can be removed by changing the correlating parameter to $\bar{\chi}_1 = \dfrac{M_1^3\sqrt{C}}{\sqrt{Re_{1,x}}}$; M_1 is the calculated Mach number for inviscid flow in the region 1 adjacent to the wedge surface and $Re_{1,x}$ is based on the characteristics of this local flow and the

distance x. The measured pressure (p_L) is now non-dimensionalised by means of the local inviscid pressure p_1. Fig. 7 shows the complete correlation of the forward-facing surface pressures for a fairly wide range of incidence ($\pm 12°$) at one test condition. Fig. 6 indicated that changes in p_∞ could be allowed for adequately, and this observation can be extended to the type of correlation shown in Fig. 7, though for clarity only points for $p_\infty = 45\mu$ have actually been included.

The line representing the correlation* is approximately

$$\frac{p_L}{p_1} = 1{\cdot}1 + 0{\cdot}33\,\bar{\chi}_1 \tag{1}$$

which is of similar general form to that suggested for predicting weak-interaction pressure increments. For example, Hayes and Probstein[6] suggest a relationship, which for zero heat-transfer, $\gamma = 1{\cdot}4$, and a Prandtl number of 0·725 reduces to

$$\frac{p_L}{p_1} = 1{\cdot}0 + 0{\cdot}35\,\bar{\chi}_1 \tag{2}$$

if second-order terms are neglected (*see* Ref. 8a on this particular point).

This method of correlation may also be applied to the case when the stream Mach number is near 2. Fig. 8a contains the mean line derived from the higher Mach-number data, and, as can be seen, the results for a range of incidence at $M_\infty = 2{\cdot}09$ fit this line reasonably well. Correlation is maintained as the free-stream pressure is dropped to 33μ and the test Mach number to 1·79; Fig. 8b shows data at two incidences (0° and +12°).

Thus by using the local flow conditions behind the leading-edge shock (or expansion) appropriate for inviscid flow, it appears possible to correlate the pressures on the forward-facing surfaces of the double-wedge aerofoil for a range of incidence and stream Mach number.

The use of local flow conditions to correlate viscous-interaction effects has of course been employed before. For example, Bertram and Blackstock[7] put forward a method suitable for hypersonic speeds and where the changes in surface slope, and hence pressure, are small. Orlik-Rückemann[10] in discussing a viscous-interaction model suitable for unsteady flows, has improved on this basic technique. The present results are perhaps of most value in demonstrating the effectiveness of the approach in conditions where the hypersonic flow approximations are not really justified, and where the flow deflections are significant.

The agreement between first-order, weak-interaction theory and experiment implicit in a comparison between equations (1) and (2) above needs to be regarded cautiously. For example, although the weak interaction mode appears to persist to values of $\bar{\chi}_1$ well in excess of those normally associated with this phenomenon, and the experimental results lie significantly below the theoretical curve predicting first-order strong-interaction effects, recent discussions (*see* Refs. 8a, 16) have tended to modify the simple distinction between weak and strong interactions, particularly if slip and so-called rarefaction effects are present. Disagreement (or agreement) with one particular theoretical model must not therefore be taken as disproving (or confirming) that model in detail.

It is thus pertinent to compare the present results with those reported by some other workers. This is done in Fig. 9, where it is seen that the present results lie between those obtained earlier. Maslach and Moulic[8a] attribute the reduced slope of their curve as $\bar{\chi}$ increases as due to the onset of strong rarefaction effects which tend to reduce the local pressure. It is generally agreed that the parameter characterising this phenomenon is $\dfrac{M\sqrt{C}}{\sqrt{Re}} \equiv \dfrac{\bar{\chi}}{M^2}$, and that values of this quantity in excess of about 0·2 lead to a reduction in induced pressure. Thus rarefaction effects should become apparent in the results of Maslach and Moulic for $\bar{\chi} > 6$. Using a similar criterion, a reduction of slope for the curve representing the results

*The data points which depart significantly from this line are mostly those for hole 2, which, for unknown reasons, gave readings which were too low (*see* Fig. 2a).

of Bertram and Blackstock would not become evident till $\bar{\chi} > 18$. Using a mean value of 4·0 as the equivalent free-stream Mach number for the majority of the NPL results, some effect from rarefaction should appear for these data near $\bar{\chi} = 3$, about the value at which they separate clearly from those due to Bertram and Blackstock. The application of such a criterion, however, becomes rather less valid at the lower Mach numbers and clearly does not apply for the results obtained near $M_\infty = 2$.

The present text is not suitable for a detailed discussion on the interpretation of pressure data obtained from flat plates; the foregoing argument has been included mainly as a warning against a too facile acceptance of the agreement between equations (1) and (2) as indication of weak-interaction phenomena. An alternative explanation may be put forward in terms of the presence of a strong interaction with some degree of slip at the surface: or perhaps these strong interaction effects are modified by merging of the shock and boundary layer to give an apparently linear relationship between p_L/p_1 and $\bar{\chi}_1$. More experimental work is clearly needed.

3.3. *Double-Wedge Section; Rearward-Facing Surfaces.*

It is apparent from Fig. 6 that the pressures over the rear part of the double-wedge section need different forms of the correlating parameters if they are to be fitted into some general pattern with those for the forward-facing surfaces. The object must be to find for these rearward surfaces the flow Mach number and static pressure of a hypothetical free stream, giving equivalent flat-plate, zero-incidence conditions, and thus determining the magnitude of the viscous-induced pressure increment. These flow quantities, designated M_2 and p_2, can be used to form a non-dimensional parameter $\bar{\chi}_2$ and p_2 used to non-dimensionalise the observed local surface pressure through the ratio p_L/p_2. The magnitude of this pressure ratio is a measure of the degree of viscous interaction present; hopefully, it would be linear with $\bar{\chi}_2$ and similar to that for the forward-facing surfaces. The length used in formulating the Reynolds number component of $\bar{\chi}_2$ is so far underfined and need not correspond to the physical surface distance from the leading edge. With these thoughts in mind, it is possible to make a very crude estimate of the way in which the boundary layer near the shoulder inhibits the attainment of the full surface expansion. The following represents an extension of a technique used earlier by Metcalf and Berry[4].

In Fig. 10 the double-wedge surface is represented by the lines $0P$ and PQ, with an expansion ϕ existing at the shoulder. The boundary layer A grows from the leading edge along the surface $0P$ and achieves a thickness δ^* at the shoulder, which is assumed to be at a distance x from the leading edge. It is now assumed that the flow along the rear surface PQ may be represented by the boundary layer labelled B whose effective origin is at $0''$, a distance s ahead of AP. It is further assumed that the characteristics of boundary layer B can be found by matching its thickness and rate of growth at P' to those of boundary layer A. Thus, at P'

$$\delta^*_A = \delta^*_B \tag{3}$$

$$\left(\frac{d\delta^*}{dx}\right)_A + \tan\phi = \left(\frac{d\delta^*}{dx}\right)_B. \tag{4}$$

The boundary-layer growth on an insulated flat plate, and hence along surface $0P$, may be represented approximately by

$$\frac{\delta^*_A}{x} = \frac{1{\cdot}73}{\sqrt{Re_{1,x}}}\left[1 + 0{\cdot}27\,M_1^2\right],$$

where M_1 is the local Mach number in the inviscid flow region 1 of Fig. 9.

Hence

$$\frac{d\delta^*_A}{dx} = \frac{1{\cdot}73}{2\sqrt{Re_{1,x}}}\left[1 + 0{\cdot}27\,M_1^2\right] = \frac{\delta^*_A}{2x}. \tag{5}$$

Equation (4) becomes

$$\frac{\delta_A^*}{2x} + \tan\phi = \frac{\delta_B^*}{2s}. \tag{6}$$

Since $\delta_A^* = \delta_B^*$, we may write

$$s = \frac{x}{1 + \dfrac{2\tan\phi}{\delta_A^*}}. \tag{7}$$

It is convenient to let

$$\delta_A^* = \frac{1{\cdot}73\sqrt{x}}{\sqrt{Re_1'}}\left[1 + 0{\cdot}27\,M_1^2\right] = G_1\sqrt{x},$$

where Re_1' is the unit Reynolds number of the local flow; G_1 is thus dependent only on known stream conditions over the front surface of the wedge (i.e. in region 1). It follows that

$$G_1\sqrt{x} = G_2\sqrt{s}, \quad \text{where} \quad G_2 = \frac{1{\cdot}73\left[1 + 0{\cdot}27\,M_2^2\right]}{\sqrt{Re_2'}}$$

and the subscript 2 denotes flow conditions appropriate to region 2 of Fig. 10. Substituting for s from equation (7), we have finally

$$G_2 = G_1\left[1 + \frac{2\sqrt{x}\tan\phi}{G_1}\right]^{1/2} \tag{8}$$

Hence G_2 is defined in terms of known quantities, the profile geometry and the flow in region 1; and since Re_2' and M_2 are uniquely related, M_2 may be found and compared with the value which would have resulted from an expansion ϕ in inviscid flow. Indeed a convenient parameter is the ratio (σ) of the effective expansion angle in viscous flow to the geometric shoulder expansion. Thus

$$\sigma = \frac{\phi_{\text{viscous}}}{\phi}.$$

The variation of σ with geometric expansion angle for $M_\infty = 4{\cdot}04$, $p_\infty = 45\mu$, at the shoulder position ($x = 0{\cdot}5$ in, 1·27 cm) of the present double-wedge aerofoil is shown in Fig. 11a. For the actual value of ϕ for this section (11.4°), σ is close to 0·6, showing that a marked under-expansion of the flow might be expected at the equivalent aerofoil incidence of 5·7°. Fig. 11b shows how σ varies with α for the double-wedge aerofoil at two stream Mach numbers of interest. In Fig. 11c the importance of the expansion position relative to the leading edge is apparent. For $\phi = 10°$ (close to the value appropriate to the double-wedge section) the full Prandtl-Meyer expansion is achieved for $x < 1{\cdot}75$ in.

Too much should not be made of quantitative predictions arising from this simple flow model, but they do suggest that correlation of the pressures over the rear surfaces of the double wedge may well be achieved by allowing for the presence of a viscous-controlled expansion; that is, an expansion at the wedge shoulder from the equivalent stream conditions M_1, p_1, is assumed but with a turning angle somewhat less than the geometric value. The results contained in Fig. 12 show rear-surface data for incidences between $-4°$ and $+20°$ at $M_\infty = 4{\cdot}04$. The broken line is the mean correlation curve for the front-surface pressures

and a reasonable degree of agreement with this can be achieved if σ is put equal to 0·5 for all incidences. Of the five points (holes 6 to 10) plotted at each incidence, one (No. 6) is exactly at the shoulder position, and this is shown as a solid symbol; correlation would not be therefore expected for this hole. Towards the rear of the section, trailing-edge interaction influences the pressure readings, causing the readings at holes 9 to 10 to be too low at small incidences and too high for large values of α. The inset to this Figure shows that for a typical incidence ($+2°$) the correlation is very poor if σ is put equal to unity, and is most satisfactory for values of σ between 0·5 and 0·6. Indeed, over all the incidence range, use of the full expansion angle fails to correlate the results along any linear curve. The best fit to the forward-facing results occurs when $\sigma \doteq 0{\cdot}55$; it is more convenient, however, to use $\sigma = 0{\cdot}50$ in subsequent analysis.

It is perhaps worth drawing attention to the low values of static pressure required for p_2, the effective stream pressure of the equivalent flat-plate flow over the rear surfaces. At $\alpha = 20°$, p_2 is $3{\cdot}7\mu$, compared with the free-stream value of 45μ. The corresponding value of M_2 is 6·20, illustrating the wide range of conditions for which correlation has been achieved. Moreover, the correlation between forward and rear surface pressures (away from the trailing edge) shown in Fig. 12 is equally good at the two other pressure levels (33μ, 65μ) for free stream Mach numbers near 4.

In Fig. 13 a similar analysis has been applied to the results obtained near $M_\infty = 2$. The trailing-edge interaction effect is more marked but apart from this correlation with the mean line for the front-surface pressures is very good at $M_\infty = 2{\cdot}09$ if a value of σ equal to 0·6 is used. One set of results at $M_\infty = 1{\cdot}79$, $p_\infty = 33\mu$ has been included to illustrate that changes in test conditions do not significantly alter the correlation at the lower test Mach numbers also.

The values of σ used in Figs. 12 and 13 (0·5 and 0·6 respectively) have been marked on the theoretical curves of Fig. 11b. They are roughly representative of some mean value over the whole incidence range of interest; it seems likely, however, that the actual variation of σ with incidence is rather smaller than that predicted by the simple theory. Nevertheless the experimental results appear to give a measure of support to the theoretical model, and hence its employment in other situations.

The pressure at the shoulder ($x/c = 0{\cdot}50$) may itself be correlated very simply by using flow conditions based on an equivalent free-stream pressure p_s, where

$$p_s = \frac{p_1 + p_2}{2}.$$

Some results for $M_\infty = 4{\cdot}04$ are shown in Fig. 14, in terms of a pressure ratio p_L/p_s and a viscous-interaction parameter $\bar{\chi}_s$. The Reynolds number used in the latter quantity is based on the distance from the leading edge to the shoulder ($c/2$).

3.4. *Biconvex Section.*

It seems reasonable to suppose that the expanding flow about the surface of the biconvex aerofoil will be subject to a similar viscous effect to that occurring downstream of the shoulder of the double-wedge profile. The actual surface pressures may perhaps best be correlated by assuming that some fraction of the local geometric expansion angle define the local equivalent flat-plate flow. Though the viscous-flow model sketched above, and indeed the concept of relating measured pressures to some flat-plate analogue, seem somewhat more doubtful for this type of flow, it is nevertheless possible to make some estimate of the likely distribution of the parameter σ along the aerofoil chord by dividing the aerofoil surface into a number of facets (Fig. 15). The junction between adjoining facets can be treated by using equation (8); in practice this means starting with the flow just behind the leading-edge shock (or expansion) and proceeding sequentially towards the trailing edge. An example showing the chordwise distribution of σ at two incidences for the conditions $M_\infty = 4{\cdot}04$, $p_\infty = 45\mu$ is shown in Fig. 15; σ now represents the effective local turning angle from the leading edge compared with the geometrical value. These results, in which the actual aerofoil surface was replaced by 10 flat segments*, suggest that a mean value of σ of around 0·7

*Very similar distributions are achieved when only five segments are employed.

may well be appropriate for the flow over the biconvex surface for a range of incidence.

The effect of variations in σ on the correlation of the actual surface pressures measured on the biconvex section is illustrated in Fig. 17. The stream conditions are $M_\infty = 4{\cdot}04$, $p_\infty = 45\mu$ and the section incidence is zero. The subscript $_3$ denotes equivalent free-stream conditions based on an expansion from just behind the leading-edge disturbance through an angle $\sigma\,\phi_L$, where ϕ_L is the local geometric expansion angle. These conditions thus define p_3, and M_3. The Reynolds number in the parameter $\bar{\chi}_3$ is also related to the distance of the pressure hole from the effective origin of the local flat-plate boundary layer (*see* Fig. 15).

When $\sigma = 1{\cdot}0$, the correlation with the data for the forward-facing surfaces is very poor, but becomes progressively better as σ is decreased until the best correlation over most of the aerofoil chord is achieved for values of σ of 0·65 or 0·70. These values are rather lower than predicted by the simple theory illustrated in Fig. 16.

The vertical scale used in Fig. 17 is a comparatively open one, and somewhat accentuates experimental scatter. Over a wide range of incidence, satisfactory correlation along a single straight line may be achieved by using $\sigma = 0{\cdot}6$, as illustrated in Fig. 18, where the vertical and horizontal scales are identical with those used in Fig. 7 for the double-wedge results. For clarity only a few incidences have been included, mostly at one free-stream condition. Changes in p_∞ and M_∞ do not affect the correlation however, and to illustrate this, data at two values of p_∞ have been included for $\alpha = +15°$.

At Mach numbers near 2, a reasonably linear correlation is achieved at 0° for $\sigma \simeq 0{\cdot}7$ (Fig. 19), suggesting that there is no large Mach number effect on this factor. For a wide range of incidence, slightly better results are obtained with σ equal to 0·6 (as at $M_\infty \simeq 4$) and this value has been used in the correlation shown in Fig. 20. The agreement between the data points and the mean line for results near $M_\infty = 4$ is very good.

A striking feature of Fig. 18 is of course the discrepancy in slope between the lines representing the two aerofoil sections; in the case of the double-wedge aerofoil this line represents both the forward-facing and the rearward-facing surfaces, using $\sigma = 0{\cdot}5$ in the latter case. The discrepancy suggests that whilst the correlating parameters (i.e. the equivalent free-stream conditions) have been correctly chosen, either the magnitude of the resultant viscous-interaction effect is markedly smaller for the biconvex section, or that there exists in this case a strong pressure gradient normal to the model surface across the thick laminar boundary layer, balancing the centrifugal effect due to the curved surface and giving a lower pressure at the solid boundary.

From the present evidence it is not possible to judge which of these factors has the most influence. It seems most likely that a major cause of the reduction in measured surface pressure is due to this normal pressure gradient. Some limited measurements of this gradient near an expansion were made by Metcalf and Berry[4]; a crude argument based on their data suggests that the pressure on the surface of the biconvex aerofoil might be only about 0·7 of that at the edge of the boundary layer. Such an effect, assuming that no such gradient exists for the double-wedge section, would account for difference in slope between the two lines of Fig. 18, but in the absence of more detailed studies this argument must only remain conjectural. It is possible however to pursue the matter a little further in a rather tentative manner by suggesting that this normal pressure-gradient effect only becomes significant when the boundary layer is thick. Thus for a hole close to the landing edge somewhat better agreement with the double-wedge line might be expected, and moreover the viscous effect causing σ to fall below unity might also be of less importance*.

In the tests at stream Mach numbers near 2, the first hole on the biconvex model was at $x/c = 0{\cdot}05$, and Fig. 21 shows that for incidences between $-12°$ and $+8°$ and for all three values of p_∞, the observed pressures agree well with the double-wedge line for the case when $\sigma = 1$. Above 8° incidence there is a progressive discrepancy between the two sets of results and it is perhaps significant that for an incidence of 10°, the lower-surface deflection is close to the maximum value for attached (inviscid) flow near $M_\infty = 2$. The non-linearity of these upper-surface results may therefore be due to shock detachment associated with the high incidence, an event which may be of less significance for more rearward holes. At $M_\infty \simeq 4$,

*The curves of Fig. 16 cannot be used as a guide to the variation of σ near the leading edge; the segmented model used is too coarse in this region.

the corresponding curve is straight up to incidences of 20° (detachment should occur for $\alpha > 27°$), but since the first hole is at $x/c = 0{\cdot}1$ in this case, the fact that its slope (with $\sigma = 1$) is smaller than that for the double-wedge aerofoil is of unknown significance. It seems possible therefore that the results contained in Fig. 21 offer some support to the argument that the magnitude of the viscous interaction at the surface is substantially modified if the solid surface is curved.

4. *Use of Correlation Curves.*

In Section 3 an attempt was made to correlate the measured pressure distributions on both the double-wedge and biconvex sections in a form similar to that for flat plates on supersonic, viscous flow. At this stage therefore it is worthwhile comparing the pressure distributions predicted from the mean correlation lines, using these over the entire aerofoil chord, with actual experimental results.

Two examples are set out in Figs. 21 and 22. In the earlier Figure, data for the double-wedge aerofoil at $\alpha = 6°$, and the stream condition $M_\infty = 4{\cdot}04$, $p_\infty = 45\mu$ have been used. In general, the agreement is satisfactory. The discrepancies towards the rear of the section are due to trailing-edge interaction and correspond to the departure of the data points from the mean correlation lines in Figs. 12 and 17 for example; even so the differences between predictions and experiments are not large. Similar test conditions apply in Fig. 22; here the agreement between prediction and experiment for the supper-surface is very good but the correlation slightly over-estimates the upper-surface pressure.

It is clear that previously suggested methods such as the 'local tangent-wedge' technique in which pressure is related directly to the combined slope of the geometric surface and the boundary-layer displacement surface would be inadequate for the biconvex section and for the rearward surfaces of the double-wedge aerofoil. Such approaches fail to allow for any viscous influence on the local flow expansions or for the effects of strong normal-pressure gradients within the boundary layer.

The correlation processes discussed in Section 3 are of course somewhat limited in scope and must be extrapolated with some caution. It is claimed, however, that they do represent a way of regarding the local flow so that its gross, viscous features are allowed for.

5. *Flow-field Explorations.*

A very limited amount of flow exploration in the neighbourhood of the model was carried out for both aerofoils, at stream conditions $M_\infty = 2{\cdot}09$, $p_\infty = 52\mu$. Traverses were made, using a pitot tube of diameter 0·125 in (3·3 mm), along lines parallel with the tunnel axis (i.e. the aerofoil chord at zero incidence). From these results, carried out at incidences of 0°, 10° and 20°, it was possible to confirm the flow Mach number upstream of the model, and to deduce approximately the shock shape and the total boundary-layer thickness (δ).

The shape of a typical pitot-tube traverse *normal* to the zero-incidence chordline (and hence obtained by cross-plotting from the actual pitot traverses) is sketched in the lower part of Fig. 24. The curve has four main components. The most inboard part (defined as $0A$) represents the boundary layer; the region AC is the non-uniform flow behind the curved shock wave. The shock wave itself corresponds to a fall in pitot pressure (CB), and because of the low stream density the shock thickness is appreciable. Outboard from point B towards D the pitot reading is constant, indicating a uniform stream, until the edge of the jet shear layer is reached.

Using the somewhat arbitrary definitions indicated in the sketch, it is possible to construct the chock shape and that of the outer edge of the boundary layer. The upper part of Fig. 24 shows results for the biconvex aerofoil at zero incidence. The shock wave is curved, and near the leading edge has a slope significantly greater than would be appropriate for inviscid flow. The shock thickness, normal to its front, appears to be about 0·15 in (3·8 mm). The use of a relatively large probe probably exaggerates this dimension; but since the shock thickness must be about 5 mean-free-paths the actual thickness cannot be less than about 0·10 in (2·5 mm).

The outer edge of the boundary layer is nearly proportional to $x^{\frac{1}{2}}$, and is in quite good agreement with an estimate based on the growth along an insulated flat plate, using the local surface Mach number and

assuming that $\delta = 2\delta^*$ (*see* Ref. 5). The significance of this agreement must not be over-stressed since both the theoretical and experimental curves contains a number of approximations. It is merely sufficient to note that the flat-plate analogue suffices here as a crude approximation. It is certainly not possible from this evidence to comment authoratively upon the experimental basis underlying the boundary-layer model sketched in Fig. 15.

Between the leading edge and $x = 0{\cdot}3$ in (7·6 mm) the regime AC in the lower sketch disappears; the shock wave and the boundary layer merge. This corresponds to $\bar{\chi}_3 > 0{\cdot}7$, and for this condition one would expect progressively increasing departures from simple weak- or strong-interaction models. The parameter correlating the onset of merging effects is $M\sqrt{C}/\sqrt{Re} = \bar{\chi}/M^2$, where these quantities are defined properly according to the local flow. For the conditions of Fig. 24 $\bar{\chi}_3/M_3^2 \simeq 0{\cdot}2$, a value in general agreement with others as indicating the beginning of merged flow (Refs. 8a, 16 for example).

The results for the double-wedge aerofoil are very similar to those contained in Fig. 24. The shock is placed in an almost identical position with respect to the chord line, whilst the boundary-layer edge is very slightly nearer the surface. This movement is small and close to the likely experimental error so that its significance is uncertain.

6. *Overall Forces on Sections.*

Though the main aim in the analysis of these aerofoil data lies in obtaining some understanding of the factors influencing the detailed pressure distribution, the overall forces acting on the two sections in low-density flow are of considerable interest, not least because information on the lift and drag of aerodynamic shapes is not plentiful in such flow conditions.

Thus the chordwise pressure distributions were integrated mechanically to produce axial and normal forces. These were reduced to coefficient form (C_X, C_N) in the usual way and subsequently resolved to provide the section lift coefficient (C_L) and the section pressure-drag coefficient (C_{D_p}). The absence of pressure holes close to the leading and trailing edges introduces some uncertainty into the determination of the axial and normal forces. This can be minimised (but not eliminated) by noting that the aerodynamic loading varies comparatively slowly along the chord and hence offers a way of extrapolating towards the leading and trailing edges. It is hoped that any residual errors will be fairly consistent so that comparisons between results obtained at different values of p_∞ and M_∞ remain valid.

The variation of C_L with incidence for the biconvex aerofoil at all test conditions is shown in Figs. 25a and b. For the incidence range covered the curves are remarkably linear with a slope appreciably greater than that predicted by the linear inviscid-flow theory*. Ref. 17 shows that at Reynolds numbers near 6×10^5 experiment and linear theory agrees very closely for both sections. The experimental curves from Figs. 25a and b are replotted in Figs. 26a and b as broken lines, where they can be compared with the experimental points for the double-wedge section. The agreement between the two section lift curves for a specific flow condition is quite remarkable, particularly when it is remembered that the viscous-induced pressure increment is essentially determined by local flow conditions and hence local geometry. The biconvex and double-wedge results at $M_\infty = 3{\cdot}95$ also agree with those obtained from balance test on a 5° single-wedge under rather similar flow conditions (Ref. 11).

In Ref. 3 it was shown that for rectangular, flat-plate wings of aspect ratio 2 at supersonic speeds, the ratio of the measured lift-curve slope to that predicted by a linear theory for inviscid flow was a linear function of $\bar{\chi}_\infty$. This curve is plotted as a broken line in Fig. 27. The experimental values of this lift-slope ratio for the biconvex and double-wedge sections lie above this line, perhaps as one might expect since they represent data for wings of infinite aspect ratio. Bertram and Henderson[12] also showed that the lift-slope ratio and $\bar{\chi}_\infty$ were related and the full line in Fig. 27 represents their theoretical prediction for both infinite aspect ratio and Mach number.

---

*Use of the correlating curves discussed in Section 3, leading to a reasonable agreement between theory and experiment for the surface pressures (as in Figs. 22 and 23), provides a good estimate of the section lift.

The fact that the lift curve slope of a wing or aerofoil increases more or less linearly with $\bar{\chi}_\infty$ amounts perhaps to little more than a recognition that all viscous-induced pressure increments on the aerofoils are linked either directly to $\bar{\chi}_\infty$ or to some modified form of this parameter, usually in a linear manner. The incremental loading at any chordwise station is thus largely independent of incidence and its magnitude depends only on some average value of $\bar{\chi}$ for the two surfaces. Since the profiles are symmetric, $\bar{\chi}_\infty$ is representative of this mean value.

The variation of axial-force coefficient with incidence is very small for all test conditions; Fig. 28 illustrates this for stream Mach numbers near 4. Since

$$C_{D_p} = C_{X_p} \cos \alpha + C_N \sin \alpha$$

it follows that over the incidence range of current interest ($\alpha \leqslant 14°$)

$$C_{D_p} \simeq (C_{D_p})_0 + C_N \sin \alpha ,$$

where $(C_{D_p})_0$ is the pressure-drag coefficient at zero incidence and the lift-dependent drag is due entirely to the normal force. This is the behaviour expected from a sharp-edged profile at supersonic speeds.

The variation of C_{D_p} with incidence at $M_\infty \simeq 4$ is given in Fig. 29a. At low incidences the biconvex aerofoil has a higher pressure drag than the double-wedge section at the same stream conditions, due to a significantly greater value of $(C_{D_p})_0$. Examples of the pressure-drag curves for stream Mach numbers near 2 have been plotted in Fig. 29b.

Tests have been made on identical aerofoil sections by Beastall and Pallant[17] at Mach numbers of 1·86 and 2·48 and at Reynolds numbers near 6×10^5. The variation of C_{D_p} with incidence for the smaller of these two Mach numbers is shown in Fig. 29b, for the double-wedge section. The shape of the curve is very similar to that obtained at low Reynolds number, but the value of $(C_{D_p})_0$ is halved.

The ratio of aerofoil lift to pressure drag is of interest in that it indicates the efficiency of the section as a lifting device. The corresponding curves from the present data are plotted in Figs. 30a and b. In general, the maximum value of C_L/C_{D_p} is little influenced by variations in stream conditions, but it has a somewhat smaller value for the biconvex aerofoil. Rather more surprisingly, the lift-to-pressure-drag ratio is almost identical in high Reynolds number flow; data from Ref. 17 are plotted in Fig. 29b for the biconvex aerofoil and similar agreement is achieved for the other aerofoil section. At small incidences at least, the increase in C_L due to interaction effects at low Reynolds numbers is balanced by the corresponding increase in $(C_{D_p})_0$, the component $C_N \sin \alpha$ being of less importance in this incidence range. It follows that the effect of Reynolds number (and also Mach number) on the maximum value of C_L/C_{D_p} is quite small.

Skin friction has of course been neglected in the foregoing, and since it can have a most significant effect in low Reynolds-number flows, it seems worthwhile making a rough estimate of its contribution to the overall section drag. Accepting that the average skin-friction coefficient on a flat plate with zero pressure gradient is given approximately by

$$C_F = \frac{1{\cdot}328}{\sqrt{Re_{\infty,c}}} \tag{9}$$

then for the flow conditions $M_\infty = 4{\cdot}04$, $p_\infty = 45\mu$, where $Re_{\infty,c} = 1170$, $C_F = 0{\cdot}0388$. The effect of viscous interaction however is to augment this value; using Ref. 13 and taking $\bar{\chi}_\infty = 2$, the new value of C_F in viscous hypersonic flow (with induced pressure gradient) becomes about 0·089. Thus the skin-friction drag coefficient for a double-sided flat plate (C_{D_F}) is about 0·180, a very large value compared with $(C_{D_p})_0$, found by experiment to be 0·0182. The revised lift/drag curve is plotted in Fig. 30a and a maximum value is no longer reached even at $\alpha = 14°$; indeed a ratio of unity is only achieved for incidences greater than 7°. By contrast, the addition of the skin-friction component at high Reynolds number would not significantly alter the lift/drag ratio.

This calculation is only intended to draw attention to the likely magnitude of skin-friction drag in

low Reynolds-number flow. The actual value of C_{D_F} quoted will be in error due to neglect of incidence and Mach number effects on C_F (*see* Ref. 12) and because of the uncertainty of applying equation (9) with accuracy at small values of $Re_{\infty,c}$ in supersonic flow. The effect of including friction drag at stream Mach numbers near 2 would be even more dramatic, since $Re_{\infty,c}$ is then many times smaller (*see* Table 1 above).

The pressure-drag coefficient at zero incidence varies with both test conditions and with aerofoil section, as the following Table shows

TABLE 2

M_∞	$p_\infty(\mu)$	$\bar{\chi}_\infty$	$Re_{\infty,c}$	Biconvex Section $(C_{D_p})_0$		Double-wedge Section $(C_{D_p})_0$	
				Experiment	Inviscid Theory	Experiment	Inviscid Theory
4·19	65	1·68	1920	0·02084	0·01486	0·0154	0·0100
4·04	45	1·93	1170	0·02410	0·01543	0·0182	0·0105
3·95	33	2·19	790	0·02830	0·01585	0·0199	0·0109
2·12	64·5	0·60	254	0·0432	0·0309	0·0297	0·0199
2·09	52	0·63	204	0·0458	0·0315	0·0312	0·0204
1·79	33	0·59	93	0·0624	0·0386	0·0420	0·0256

The viscous-induced pressure-drag increment is about the same for the two aerofoils at a given flow condition, but neither this quantity, nor the ratio of the experimental to the inviscid pressure drag correlate well when plotted against $\bar{\chi}_\infty$. Indeed because the local pressure ratio $\left(\frac{p_L}{p_\infty}-1\right)$ is proportional to $\bar{\chi}_\infty$ (or some variant of this), one can argue approximately that when integrating around the profile to find the pressure drag

$$\oint \left(\frac{p_L}{p_\infty}-1\right) d\left(\frac{y}{c}\right) \propto C_{D_p} . M_\infty^2 \propto \bar{\chi}_\infty + \text{constant}$$

since

$$\tfrac{1}{2}\rho_\infty U_\infty^2 = \tfrac{1}{2}\gamma p_\infty M_\infty^2 .$$

The resulting correlation for zero incidence is shown in Fig. 31; well-defined curves exist for both sections.

An alternative, yet to all appearances quite satisfactory, correlation can be achieved simply by plotting $(C_{D_p})_0$ against test Reynolds number $(Re_{\infty,c})$, as in Fig. 32; test Mach number then seems to be unimportant, though admittedly the variation in M_∞ is not large for each group of points. However, Potter[14] has produced a similar correlation for sharp and blunt-nosed cones over a wide range of stream Mach number. The absence of a strong Mach number effect suggests that an effective blunt-body flow exists in the leading edge region associated with the rapidly thickening boundary layers (as indeed is suggested by Fig. 24). The pressure drag is then dominated by this feature.

7. *Concluding Remarks.*

This report has been concerned with an analysis of the surface pressures on two different aerofoil sections for stream Mach numbers between 1·79 and 4·19, and for a range of stream static pressures.

It has been demonstrated that for a plane surface inclined to the flow direction (the front surfaces of the double-wedge aerofoil) the local pressures may be correlated adequately by means of a viscous-interaction parameter $\bar{\chi}_1$ based on conditions near the wedge surface in inviscid flow. The rearward surfaces of the double-wedge section, however, are influenced by the shoulder expansion and the pressures on these surfaces correlate well only if it is assumed that the presence of a thick laminar boundary layer prevents the attainment of the full Prandtl-Meyer expansion at the shoulder. A similar constraint on the magnitude of the flow expansion applies to the biconvex section. The flow models used in estimating the likely size of the viscous-controlled expansion are very simple and are not likely to represent at all closely the real boundary-layer flow in either a local, or a continuous, expansion. The theoretical predictions are, however, roughly in accord with the experimental data.

The general phenomenon of a thick viscous layer inhibiting a surface expansion is of considerable importance, and its neglect could well lead to significant errors on the calculation of body forces, control-surface effectiveness and other aerodynamic information. It follows that more experimental work is required to investigate the influence of surface geometry on the process, and on the static pressure gradient normal to the surface thought to be responsible in the present tests for the discrepancy between the correlation of the biconvex and double-wedge surface pressures. That these pressures can in fact be correlated over a wide range of Mach number and Reynolds number appears to indicate an underlying unity in the mechanisms dominating viscous interactions, even though the nature of such mechanisms is at present only dimly perceived.

The effect of the viscous-induced pressure increments on the section lift and drag is most dramatic. Lift-curve slopes well in excess of the inviscid (and hence high Reynolds number) values can be achieved, but these are accompanied by high pressure-drags, so that the ratio of lift to pressure-drag is almost identical to that produced at high Reynolds numbers. At low Reynolds numbers, however, the skin-friction drag is extremely large, and represents a major part of the overall section drag. Its inclusion results in a lift-drag ratio near $M_\infty = 4$ that does not exceed unity until the aerofoil incidence is greater than 7°; at lower Mach numbers, because the Reynolds numbers are smaller, the ratio unity is not reached over the test range of interest.

The section lift and drag characteristics give some indication of the type of aerodynamic behaviour likely from lifting-surfaces in rarefied, low-Reynolds-number flow. High aerodynamic efficiency is likely to be most difficult to attain, and indeed it may not always be a flight requirement. Nevertheless an understanding of the factors contributing to and controlling the overall aerodynamics of a wing or body flying at high altitude is a basic necessity and it is hoped that the present text represents a small contribution towards this objective.

LIST OF SYMBOLS

AR	Aspect ratio of wing
C_N, C_X	Normal force, axial-force coefficients
C_L, C_D	Lift, drag coefficients
C_{D_p}	Pressure-drag coefficient
$(C_{D_p})_0$	Value of C_{D_p} at $\alpha = 0°$
C_F	Average skin-friction coefficient on a flat plate
C_{DF}	Skin-friction drag of aerofoil
C	Chapman-Rubesin factor $\left(= \frac{\eta_w}{\eta_\infty} \cdot \frac{T_\infty}{T_w} \right)$, where η is fluid viscosity and subscripts '∞' and 'w' refer to free-stream and wall conditions.
G_n	$\frac{1{\cdot}73}{\sqrt{Re'}} \left[1 + 0{\cdot}27\, M_n^2 \right], n = 1, 2, \ldots$
M_∞	Free-stream Mach number
M_1	Mach number of inviscid flow adjacent to forward-facing surfaces of double-wedge section (Region 1)
M_2	Mach number of equivalent free-stream flow adjacent to rearward-facing surfaces of double-wedge section (Region 2)
M_x	Mach number at position x
M_s	Mach number of equivalent free-stream flow for shoulder position of double-wedge section
$R_{e^{\infty, c}}$	Reynolds number based on stream conditions and model chord
$Re_{\infty, x}$	Reynolds number based on stream conditions and distance x
$Re_{1, x}$	Reynolds number based on flow conditions in Region 1, and distance x (double-wedge section)
$Re_{2, s}$	Reynolds number based on flow conditions in Region 2, and distance s (double-wedge section)
$Re_{3, x}$	Reynolds number based on flow conditions in Region 3, and distance x (biconvex section)
Re_s	Reynolds number based on flow conditions in equivalent free-stream for shoulder position (double-wedge section) and distance $c/2$
$Re'_n (n = 1, 2, 3)$	Unit Reynolds number in Regions 1, 2, 3 ...
U_∞	Free-stream velocity
c	Aerofoil chord
p_L	Local (measured) pressure on aerofoil surface
p_∞	Free-stream pressure
p_1, p_2, p_3	Equivalent free-stream pressures in Regions 1, 2, 3

LIST OF SYMBOLS—*continued*

p_s Pressure of equivalent free-stream for shoulder position (double-wedge section)

s Distance upstream of shoulder of origin for equivalent boundary layer flowing along rearward-facing surfaces of double-wedge section (*see* Fig. 10)

x Distance along aerofoil chord-line from leading edge

y Distance normal to aerofoil chord-line

α Aerofoil incidence

$\delta^*, \delta_A^*, \delta_B^*$ Boundary-layer displacement thicknesses (*see* Fig. 10)

δ Total boundary-layer thickness

μ Pressure of 1 millitorr

σ Ratio of effective to geometric expansion angles

ϕ Expansion angle at shoulder of double-wedge section

ϕ_L Local expansion angle, measured from leading edge, on surface of biconvex aerofoil

ρ_∞ Free-stream density

γ Ratio of specific heats of test gas (= 1·40 for air)

$\bar{\chi}_\infty$ Viscous-interaction parameter $\left(= \dfrac{M_\infty^3 \sqrt{C}}{\sqrt{Re_{\infty, c}}} \right)$

$\bar{\chi}_0$ Viscous-interaction parameter $\left(= \dfrac{M_\infty^3 \sqrt{C}}{\sqrt{Re_{\infty, x}}} \right)$

$\bar{\chi}_1$ Viscous-interaction parameter $\left(= \dfrac{M_1^3 \sqrt{C}}{\sqrt{Re_{1, x}}} \right)$

$\bar{\chi}_2$ Viscous-interaction parameter $\left(= \dfrac{M_2^3 \sqrt{C}}{\sqrt{Re_{2, s}}} \right)$

$\bar{\chi}_3$ Viscous-interaction parameter $\left(= \dfrac{M_3^3 \sqrt{C}}{\sqrt{Re_{3, x}}} \right)$

$\bar{\chi}_s$ Viscous-interaction parameter $\left(= \dfrac{M_s^3 \sqrt{C}}{Re_s} \right)$

REFERENCES

No.	*Author(s)*	*Title, etc.*
1	E. W. E. Rogers, C. J. Berry and B. M. Davis	Experiments with cones in low-density flows at Mach numbers near 2. A.R.C. R. & M. 3505. 1964.
2	S. C. Metcalf, C. J. Berry and B. M. Davis	An investigation of the flow about circular cylinders placed normal to a low-density supersonic steam. A.R.C. R. & M. 3416. 1964.
3	E. W. E. Rogers and S. C. Metcalf	AGARDograph 97, Part 2, pp 968–985. 1965.
4	S. C. Metcalf and C. J. Berry	Boundary-layer interaction effects in low-density supersonic flow. *Proc. 5th Int. Symp. on Rarefied Gas Dynamics.* Vol. II (Ed: C. Brundin), pp 1087–1106. 1966.
5	E. W. E. Rogers, C. J. Berry and B. M. Davis	An experiment investigation of the interaction between a forward-facing step and a laminar boundary layer in supersonic low-density flow. A.R.C. R. & M. 3506. 1965.
6	W. D. Hayes and R. F. Probstein	*Hypersonic Flow Theory.* Academic Press. 1956.
7	M. H. Bertram and T. A. Blackstock	Some simple solutions to the problem of predicting boundary-layer self-induced pressures. NASA Tech. Note D–798. 1961.
8a	E. S. Moulic and G. J. Maslach	Induced pressure measurements on an insulated sharp-edged flat plate in low-density hypersonic flow. *Proc. 5th Int. Symp. on Rarefied Gas Dynamics*, Oxford. (Ed: C. L. Brundin). Academic Press. pp. 971–992. 1967.
8b	M. Becker and D. Boylan	Experimental flow field investigations near the sharp edge of a cooled flat-plate in a hypervelocity, low-density flow. pp. 993–1014.
8c	I. E. Vas and J. Allegre	The N–4 low-density facility and some preliminary results on a sharp flat plate. pp. 1014–1030.
8d	W. J. McCrosky, S. M. Bogdonoff and A. P. Genchi	Leading edge flow studies of sharp bodies in rarefied hypersonic flow. pp. 1047–1066.
9	R. L. Chuan and S. A. Waiter	Experimental study of hypersonic rarefied flow near the leading edge of a thin flat plate. *Proc. 3rd Int. Symp. on Rarefied Gas Dynamics*, Paris (Ed: J. L. Laumann). Academic Press, pp 328–342. 1963.
10	J. Orlik-Rückemann	Stability derivatives of sharp wedges in viscous hypersonic flow. NCR (Canada) Aero Report LR–431. 1965.

REFERENCES—*continued*

No.	*Author(s)*	*Title, etc.*
11	S. A. Schaaf, E. S. Moulic, M. T. Chahine and G. J. Maslach	Aerodynamic characteristics of wedges in low-density supersonic flow. Univ. Calif. Tech. Rep. HE–150–180. 1960.
12	M. H. Bertram and A. Henderson	Effects of boundary-layer displacement and leading-edge bluntness on pressure distribution, skin friction and heat transfer of bodies at hypersonic speeds. NACA TN 4301. 1958.
13	M. H. Bertram	Boundary-layer displacement effects in air at Mach numbers of 6·8 and 9·6. NASA TR R–22. 1959.
14	L. Potter	The transitional rarefied-flow regime. *Proc. 5th Int. Symp. Rarefied Gas Dynamics*, Oxford. (Ed: C. L. Brundin). Academic Press. pp. 881–937. 1967.
15	J. M. Kendall	An experimental investigation of leading-edge shock-wave—boundary-layer interaction at Mach 5·8. *J. Aero Sci., 24*, pp. 47–56. 1957.
17	S. C. Metcalf, D. C. Millicrap and C. J. Berry	A study of the effect of surface condition on the shock-layer development over sharp-edged shapes in low Reynolds number high speed flow. Paper given at the *6th Int. Symp. on Rarefied Gas Dynamics*, Boston. 1968.
17	D. Beastall and R. J. Pallant	Wind tunnel tests on two-dimensional supersonic aerofoils at $M = 1{\cdot}86$ and $M = 2{\cdot}48$. A.R.C. R. & M. 2800, 1950.

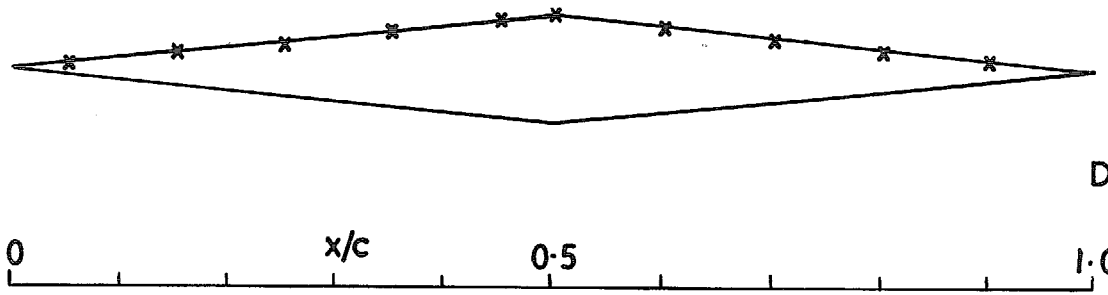

Hole No	x/c A	x/c B
1	0·05	0·10
2	0·15	0·20
3	0·25	0·30
4	0·35	0·40
5	0·45	0·50
6	0·50	0·55
7	0·60	0·65
8	0·70	0·75
9	0·80	0·85
10	0·90	0·95

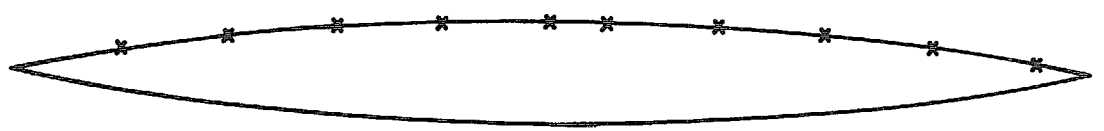

A { Wedge at $M_\infty \triangleq 4$
Biconvex at $M_\infty \triangleq 2$

B { Wedge at $M_\infty \triangleq 2$
Biconvex at $M_\infty \triangleq 4$

The leading and trailing edges were defined differently in these two cases.

FIG. 1. Aerofoil profiles.

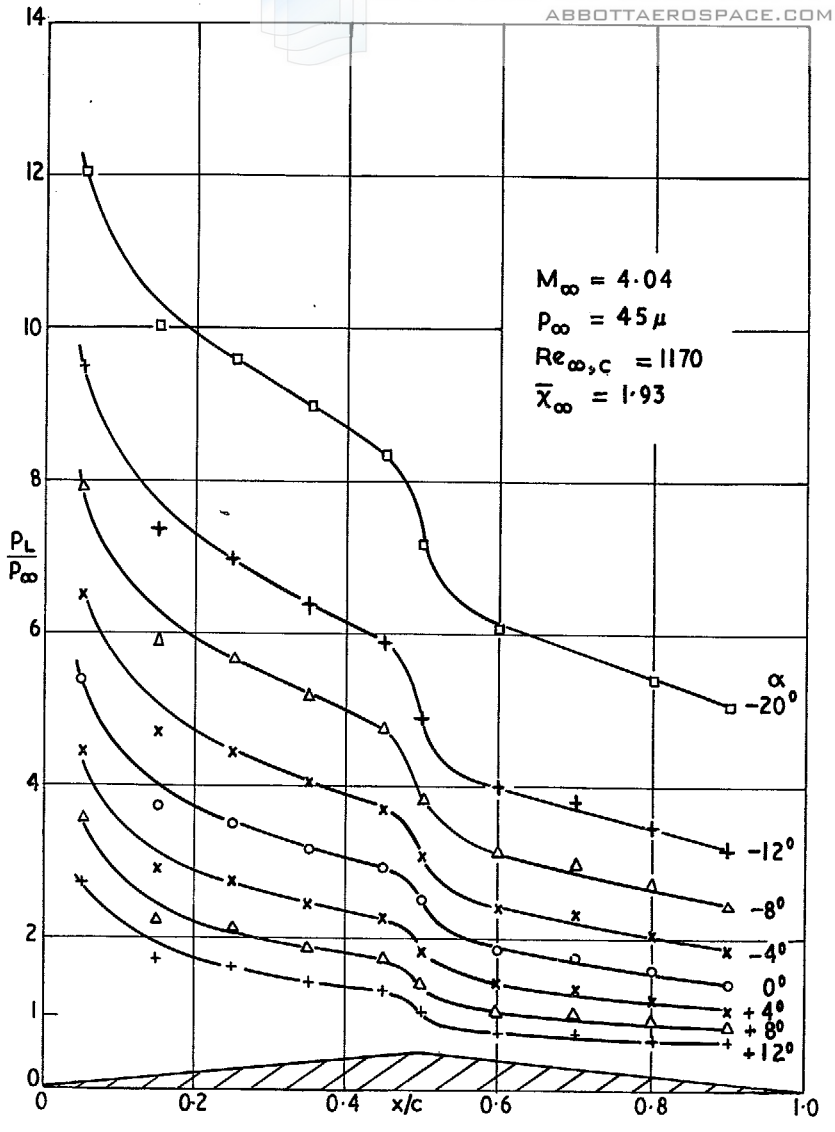

FIG. 2a. Pressure distributions on double-wedge aerofoil at $M_\infty = 4{\cdot}04$. (Upper surface).

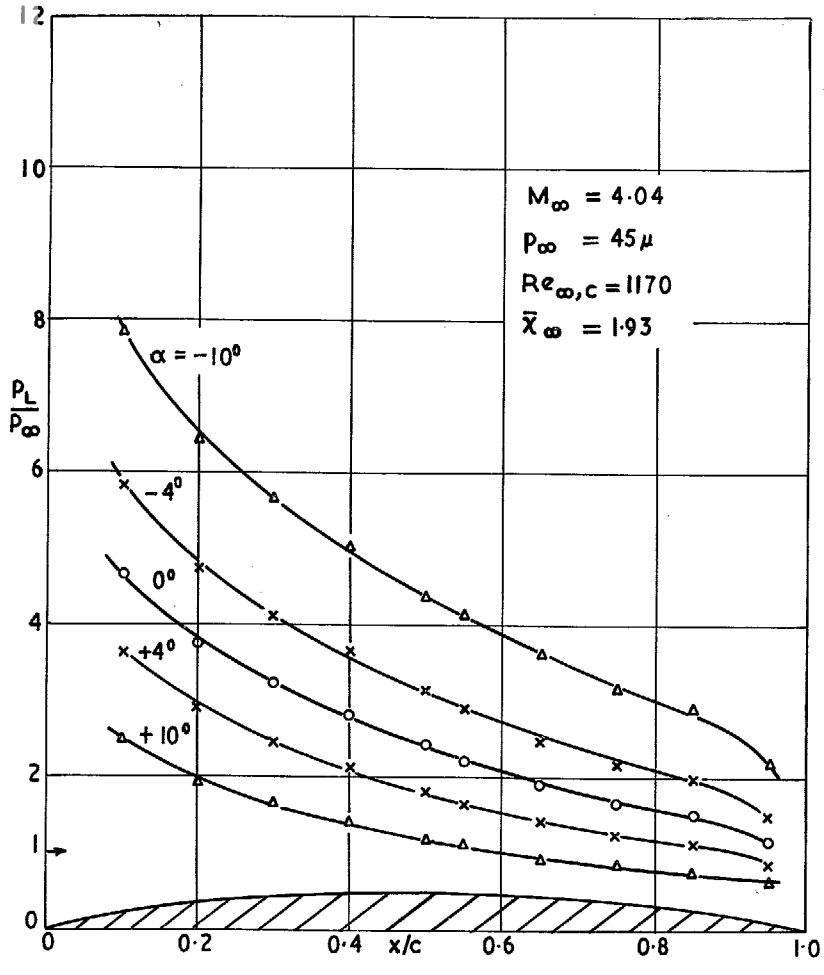

FIG. 2b. Pressure distribution on biconvex aerofoil at $M_\infty = 4{\cdot}04$. (Upper surface).

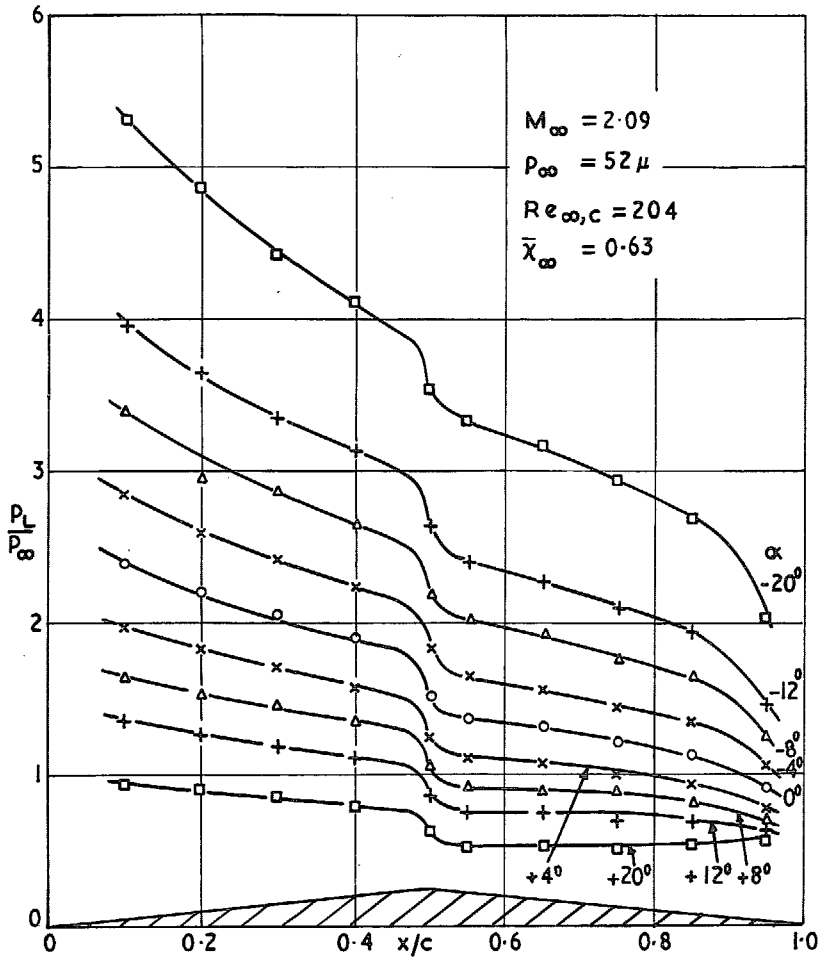

FIG. 3a. Pressure distribution on double-wedge aerofoil at $M_\infty = 2{\cdot}09$. (Upper surface).

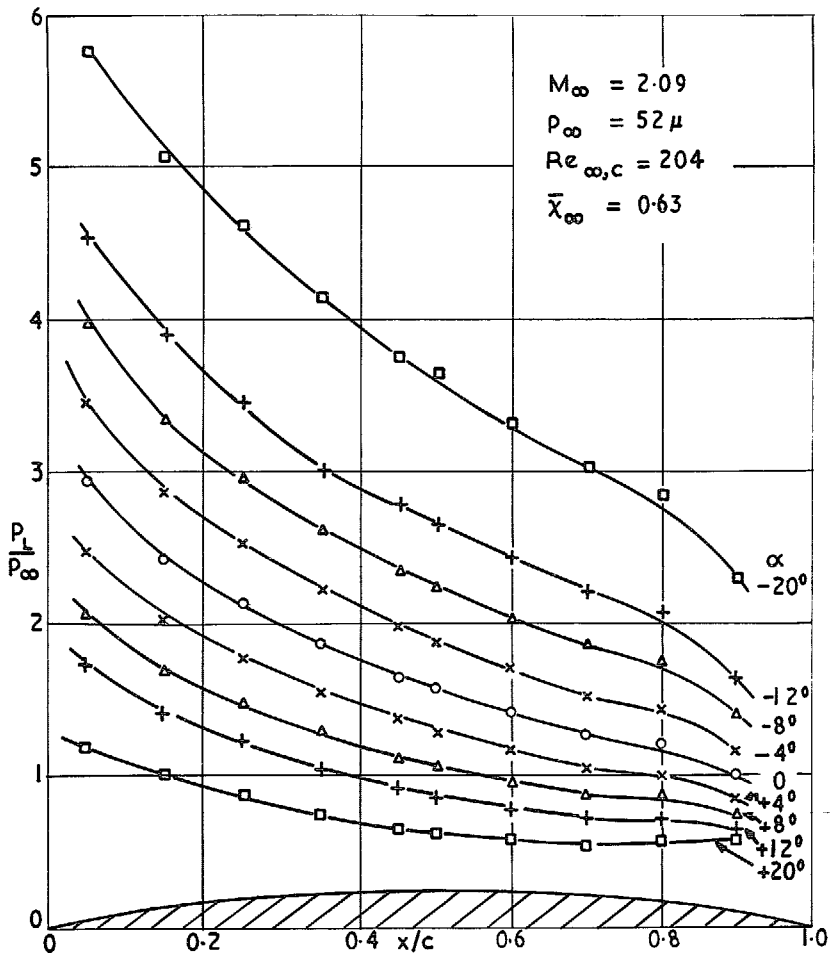

FIG. 3b. Pressure distribution on biconvex aerofoil at $M_\infty = 2{\cdot}09$. (Upper surface).

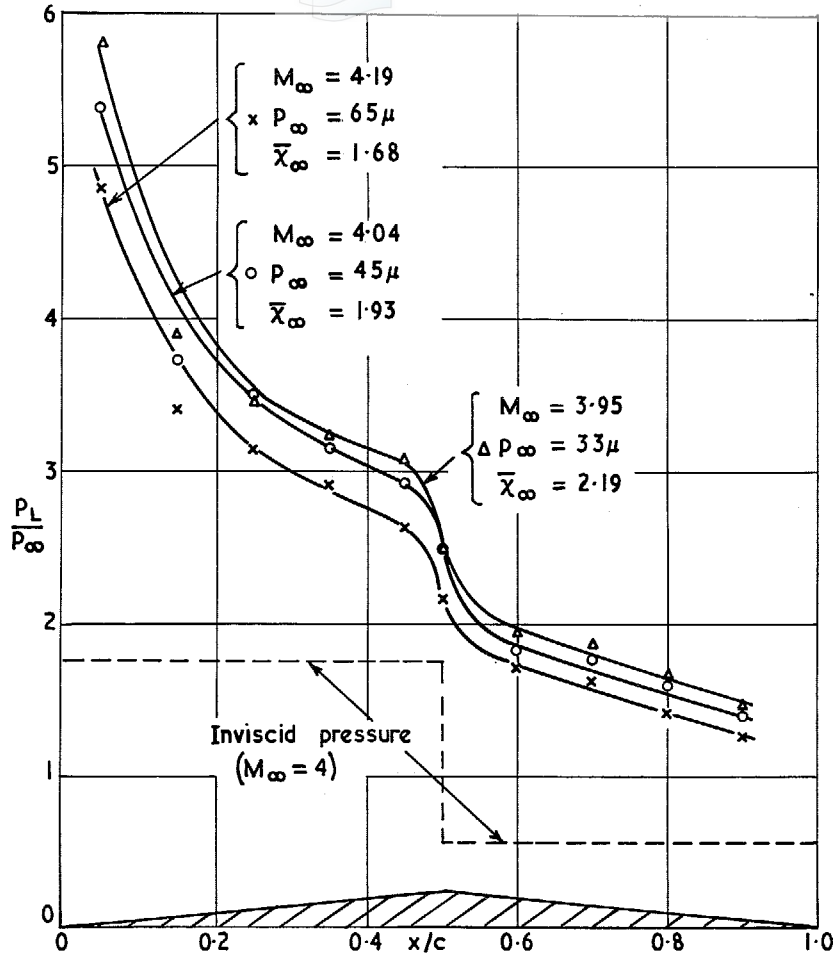

FIG. 4a. Influence of test static pressure and stream Mach number on surface pressures of double-wedge aerofoil at $\alpha = 0°$; $M_\infty \simeq 4$.

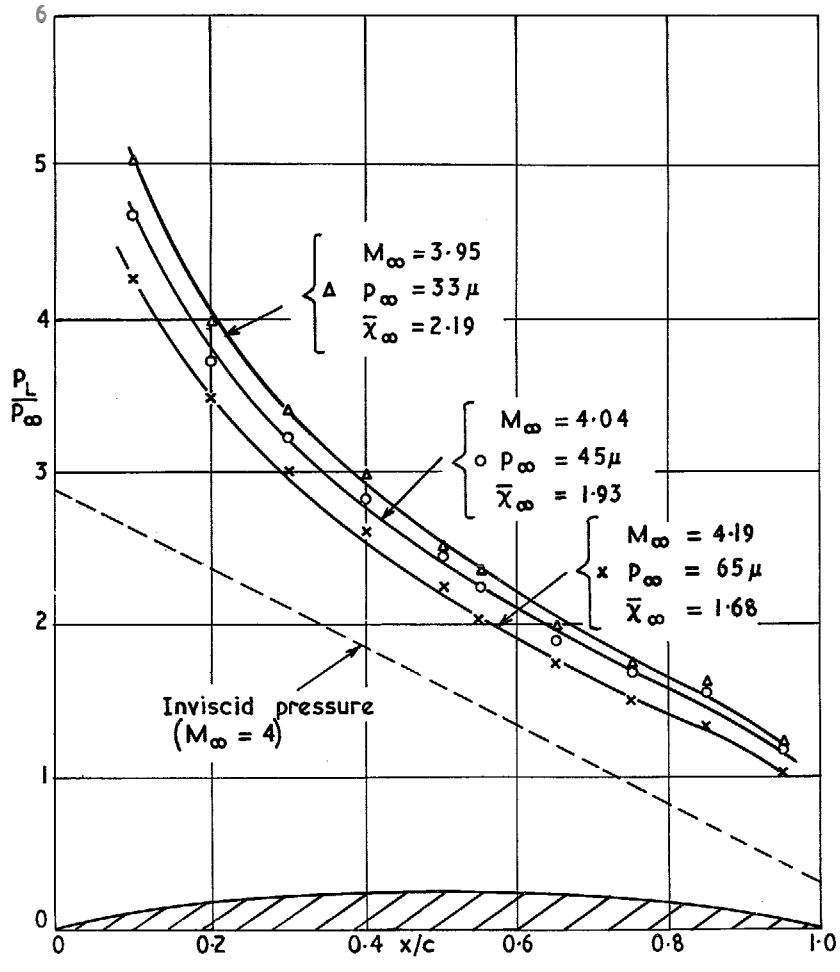

FIG. 4b. Influence of test static pressure and stream Mach number on surface pressures of biconvex aerofoil at $\alpha = 0°$; $M_\infty \simeq 4$.

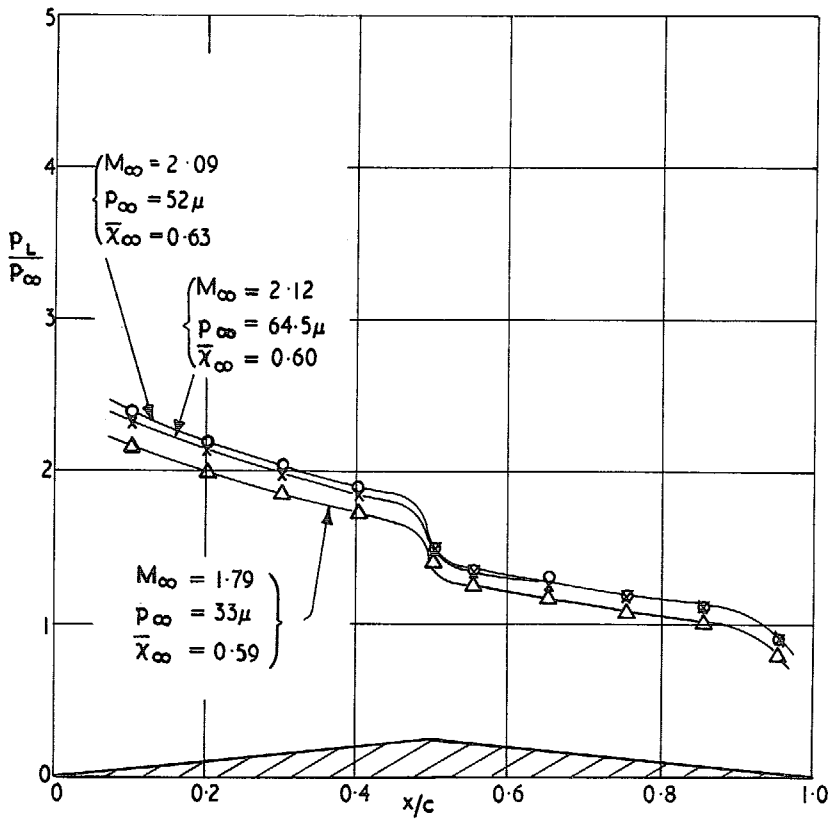

FIG. 5a. Effect of stream Mach number and static pressure change on pressure distribution for double-wedge aerofoil at $\alpha = 0°$; $M_\infty \doteq 2$.

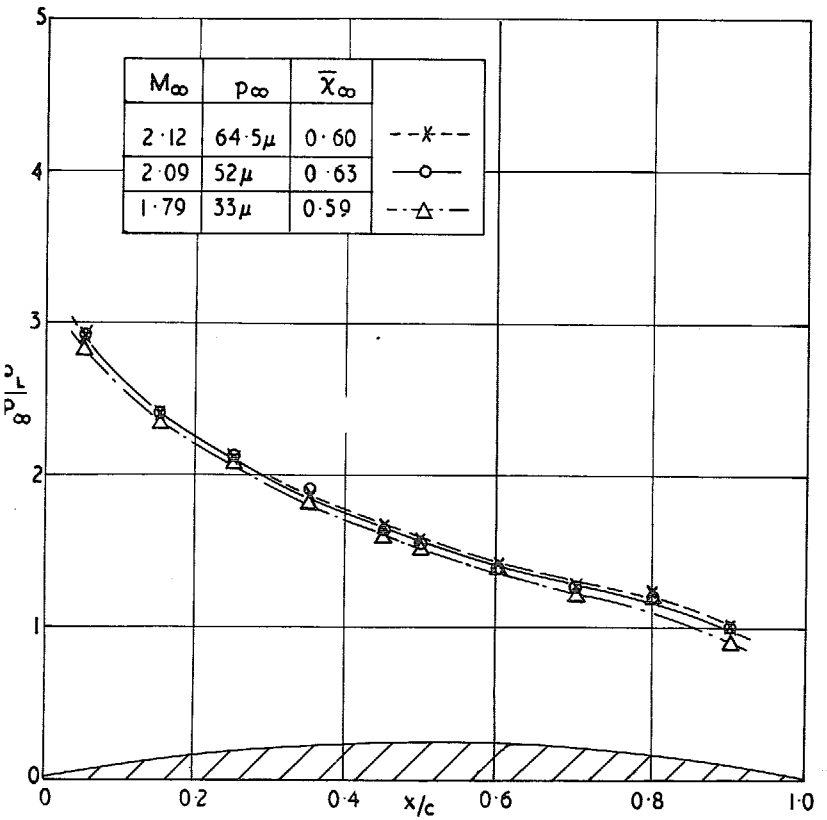

FIG. 5b. Effect of stream Mach number and static pressure change on pressure distribution for biconvex aerofoil at $\alpha = 0°$; $M_\infty \doteq 2$.

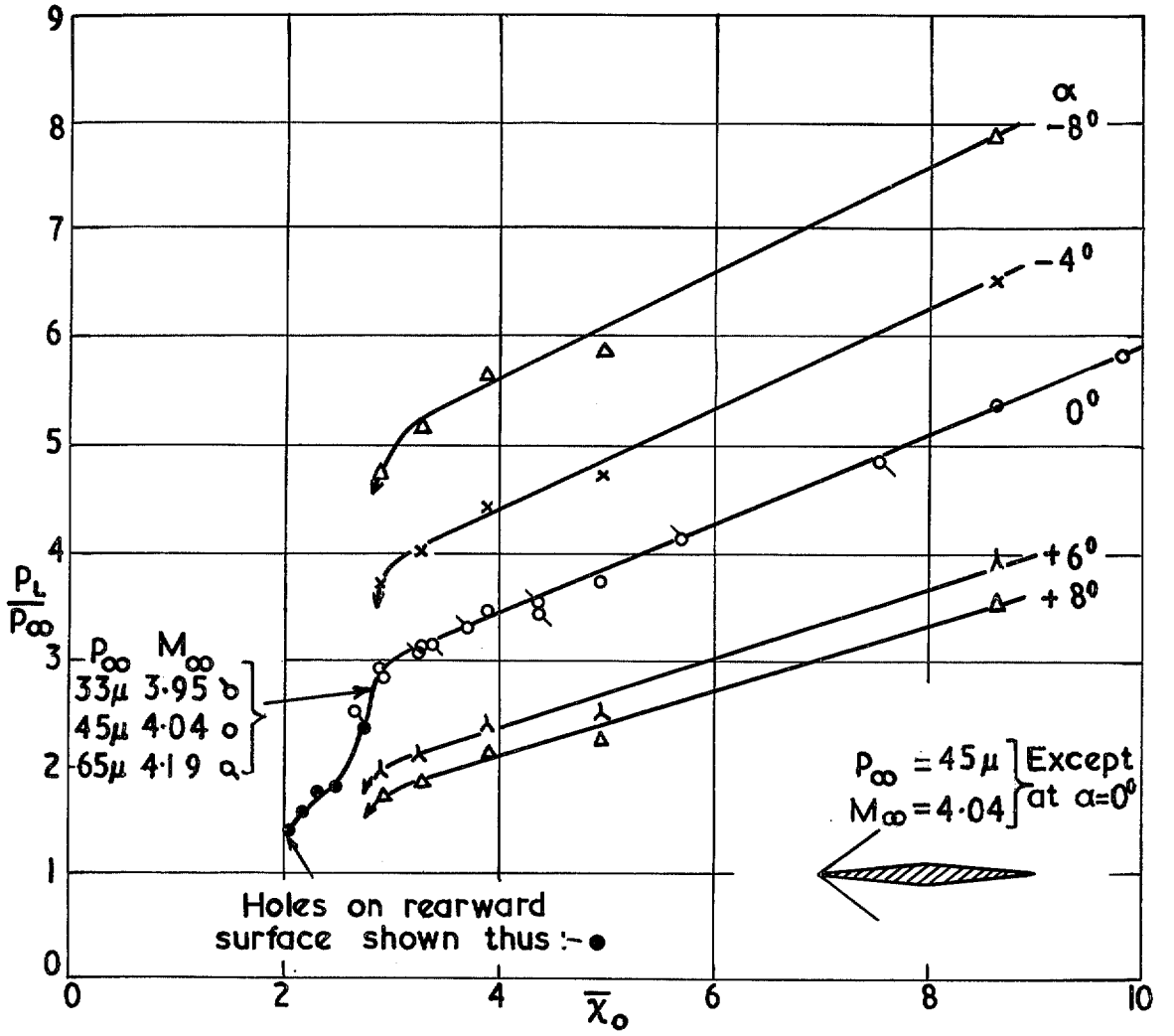

FIG. 6. Effect of incidence on pressure correlation for forward-facing surface with viscous-interaction parameter (double wedge).

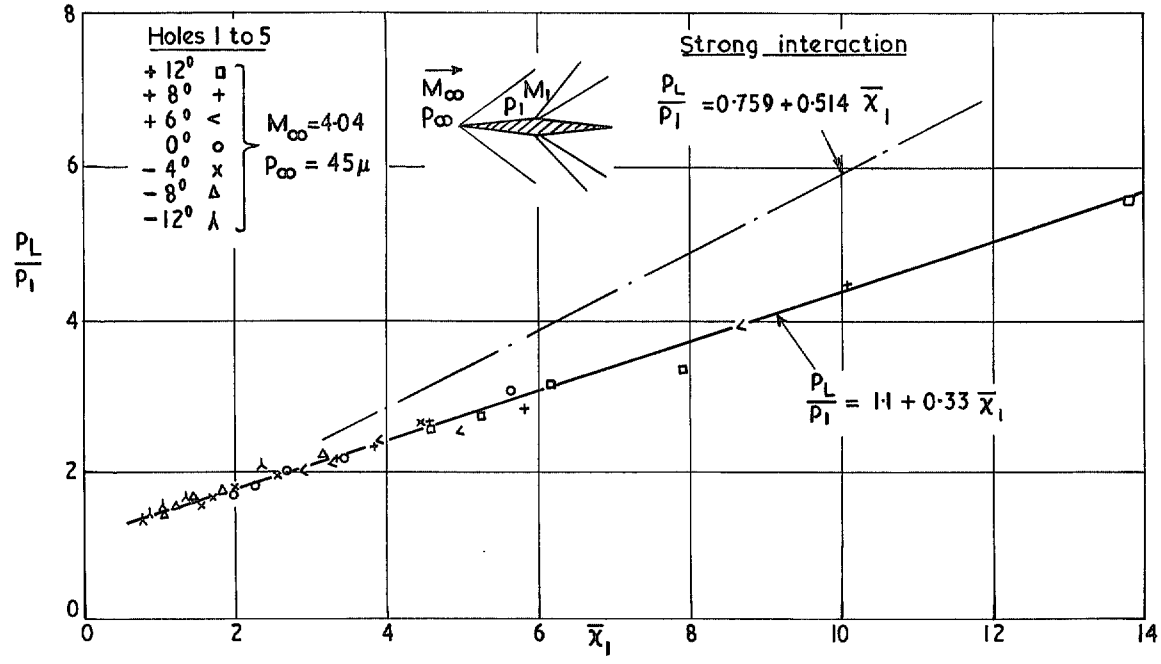

FIG. 7. Correlation of front-surface pressures on double-wedge aerofoil for $M_\infty = 4{\cdot}04$.

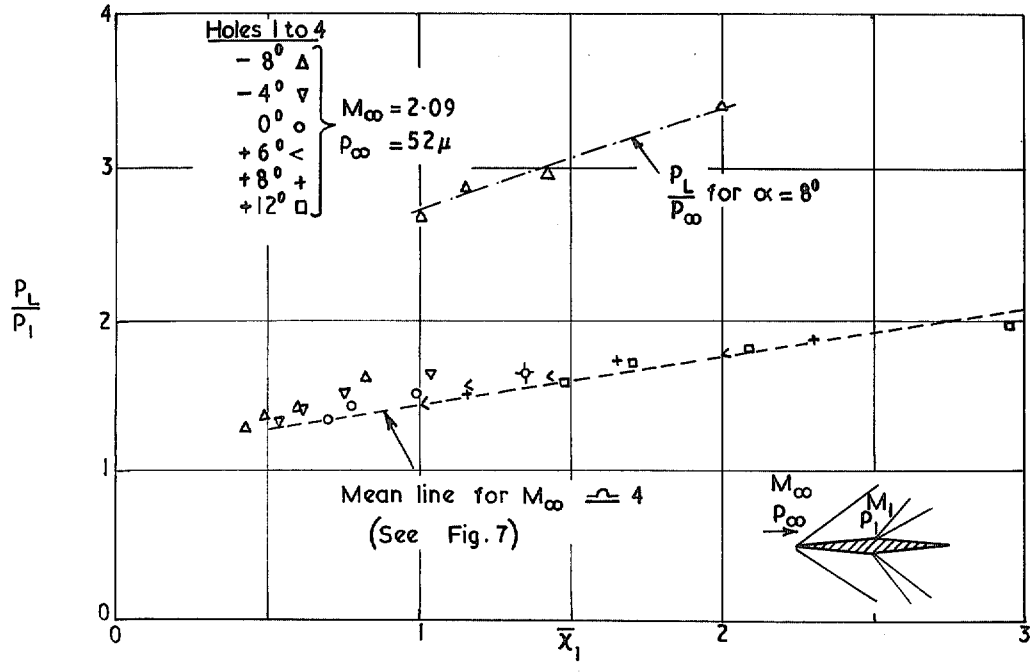

FIG. 8a. Correlation of front-surface pressures on double-wedge aerofoil for $M_\infty = 2{\cdot}09$.

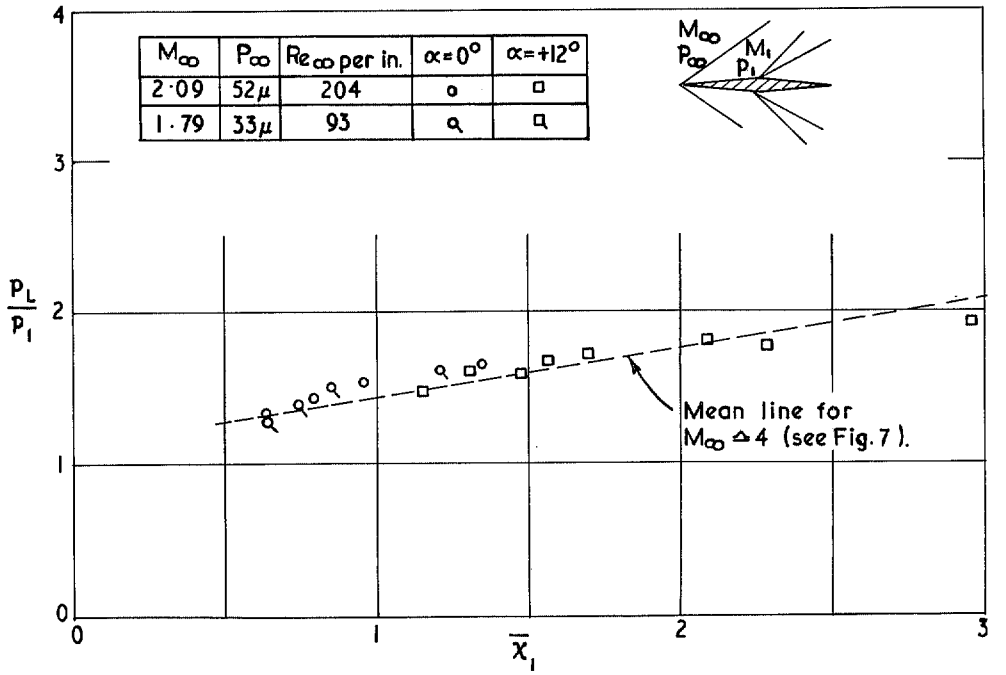

FIG. 8b. Effect of stream Mach number and static-pressure changes on front-surface correlation for $M_\infty \simeq 2$.

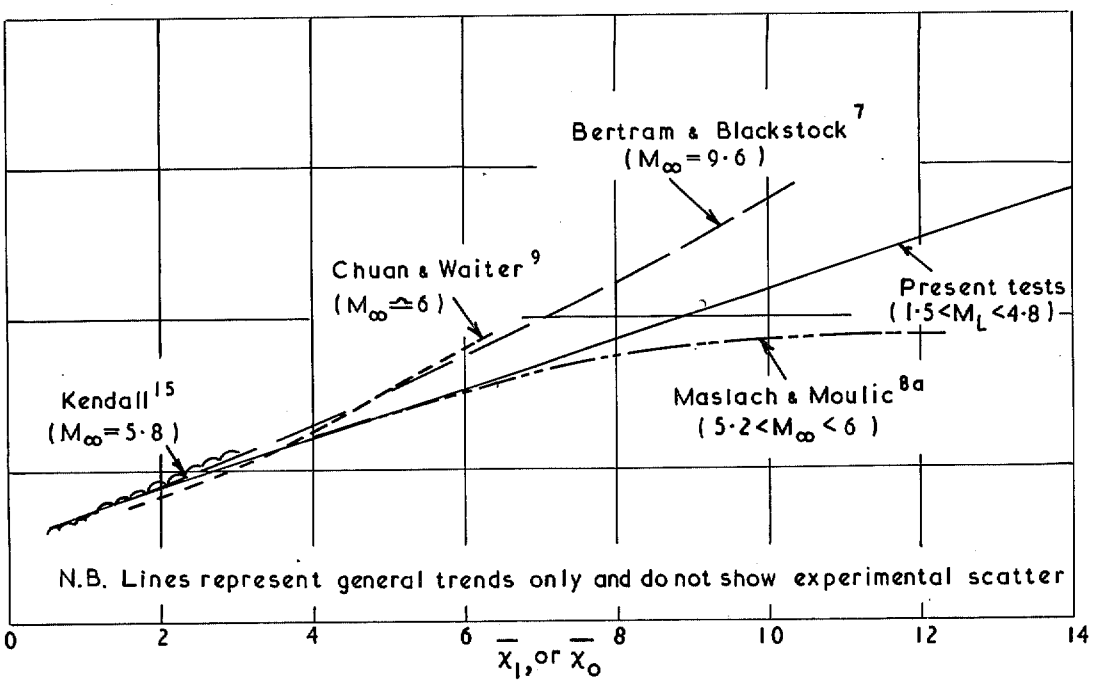

FIG. 9. Viscous-induced pressures on flat, insulated surfaces (sharp leading edge) at moderate hypersonic speeds in air.

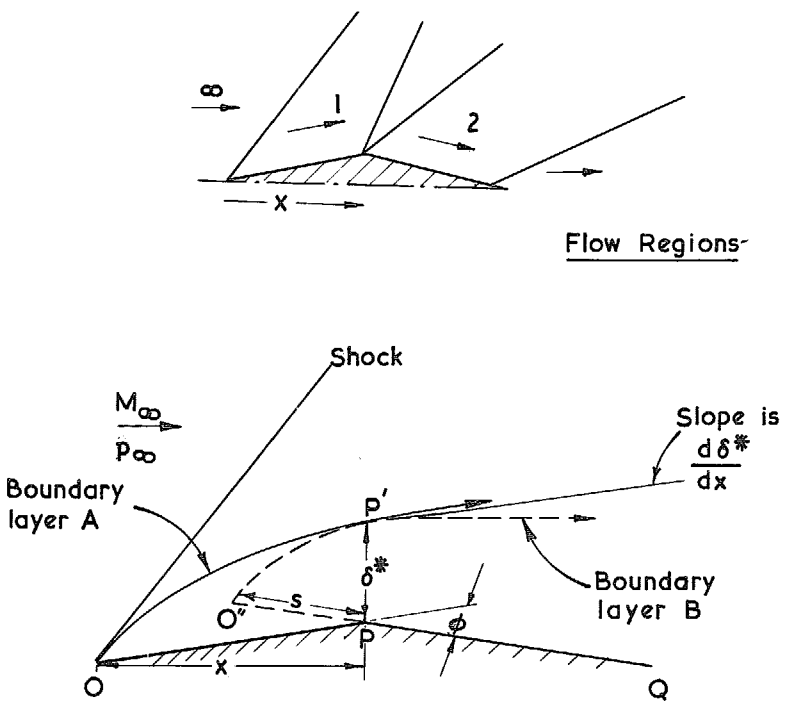

FIG. 10. Model of Boundary-layer flow at shoulder.

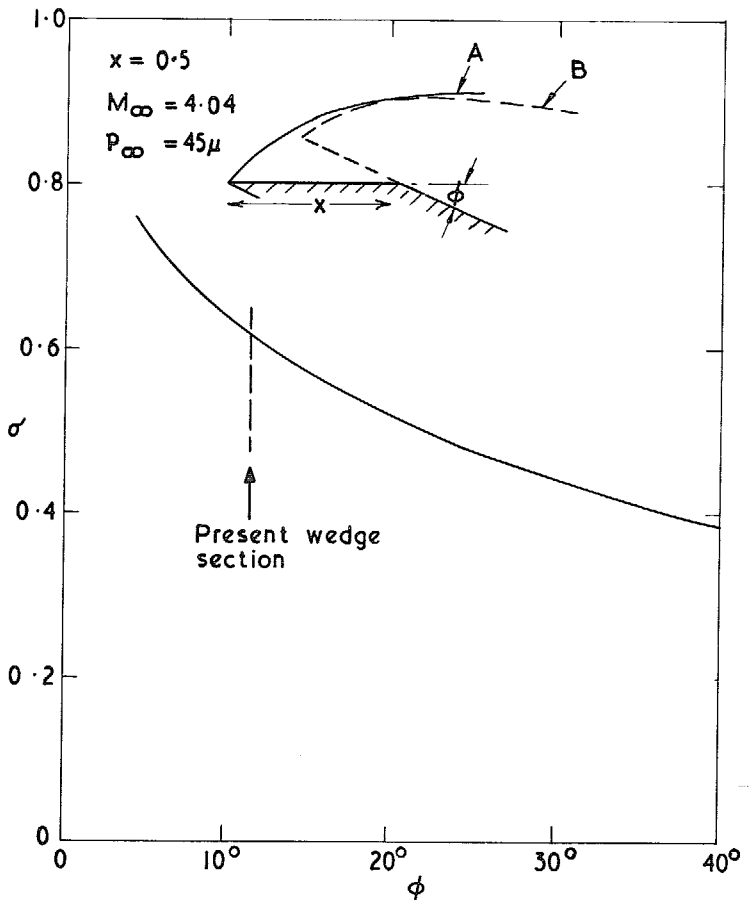

FIG. 11a. Influence of flow deflection on σ at constant M_∞, p_∞ and shoulder position.

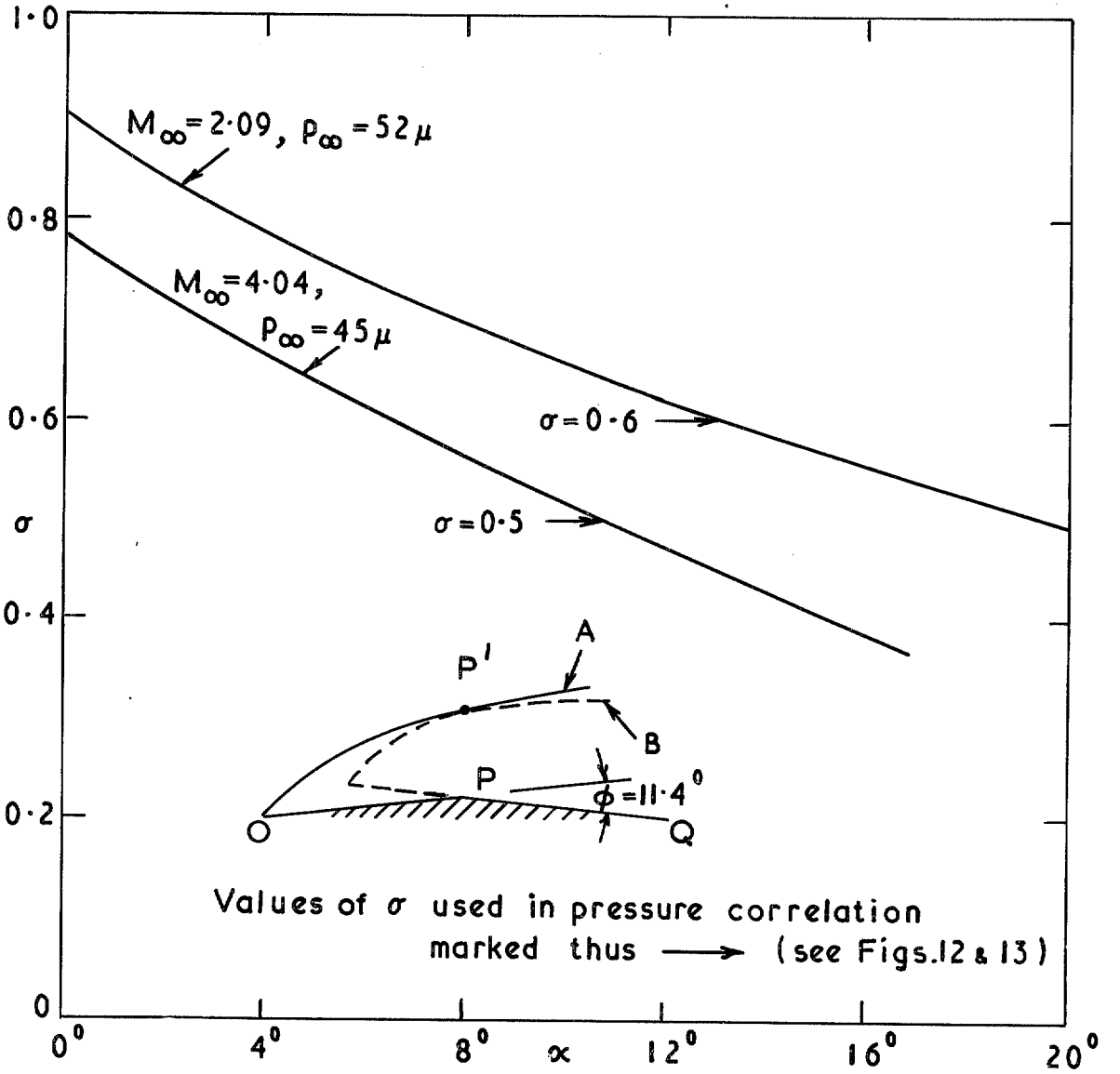

FIG. 11b. Values of σ predicted for double-wedge aerofoil from matching boundary-layers at shoulder.

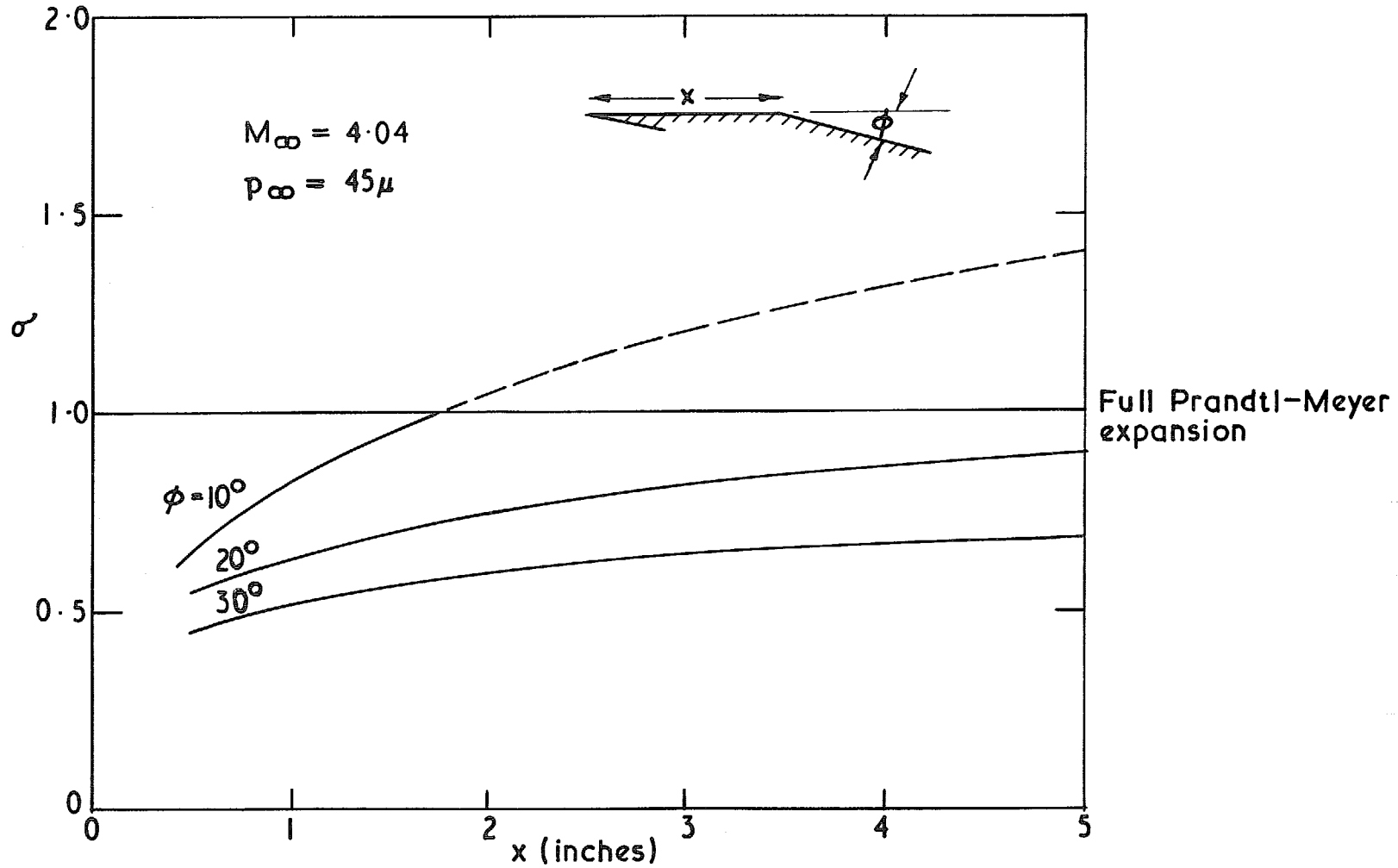

FIG. 11c. Influence of shoulder position on σ at constant M_∞.

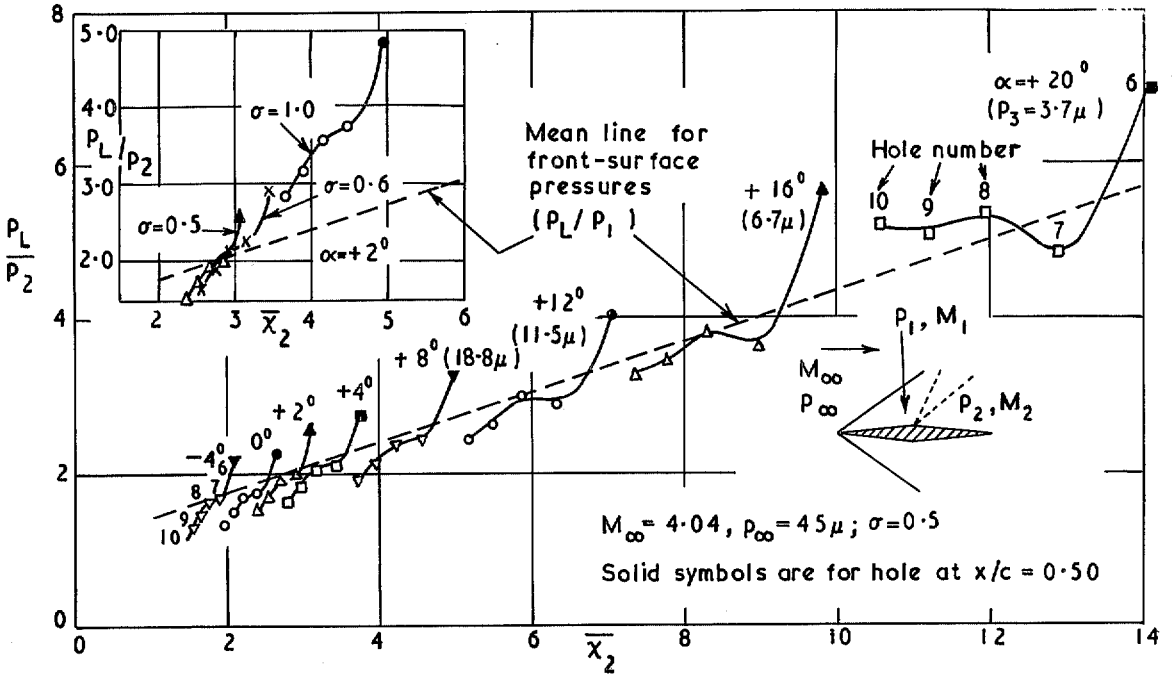

FIG. 12. Correlation of rear-surface pressures on double-wedge aerofoil for $M_\infty = 4{\cdot}04$.

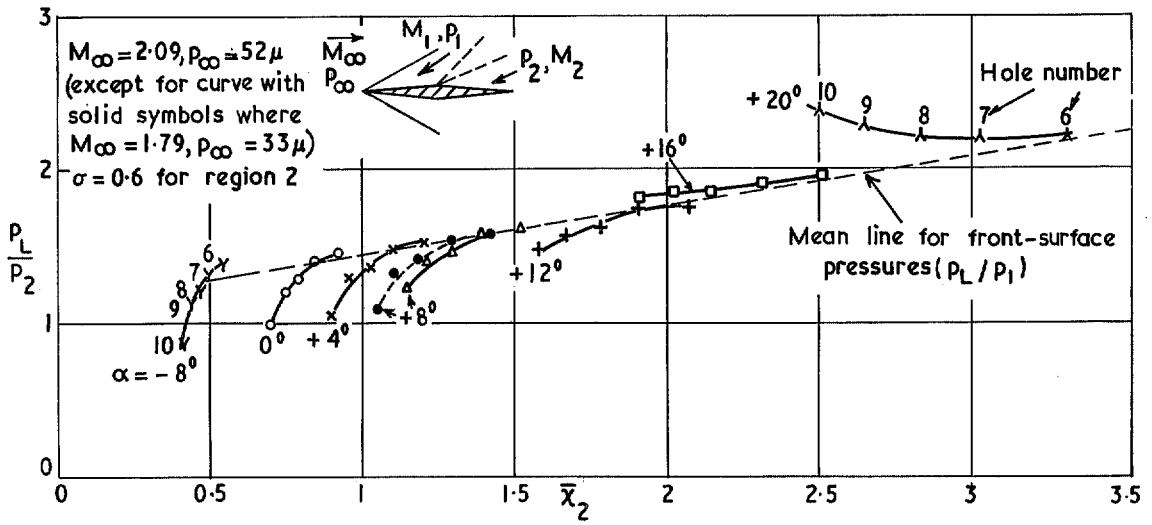

FIG. 13. Correlation of rear-surface pressures on double-wedge aerofoil for $M_\infty \simeq 2$.

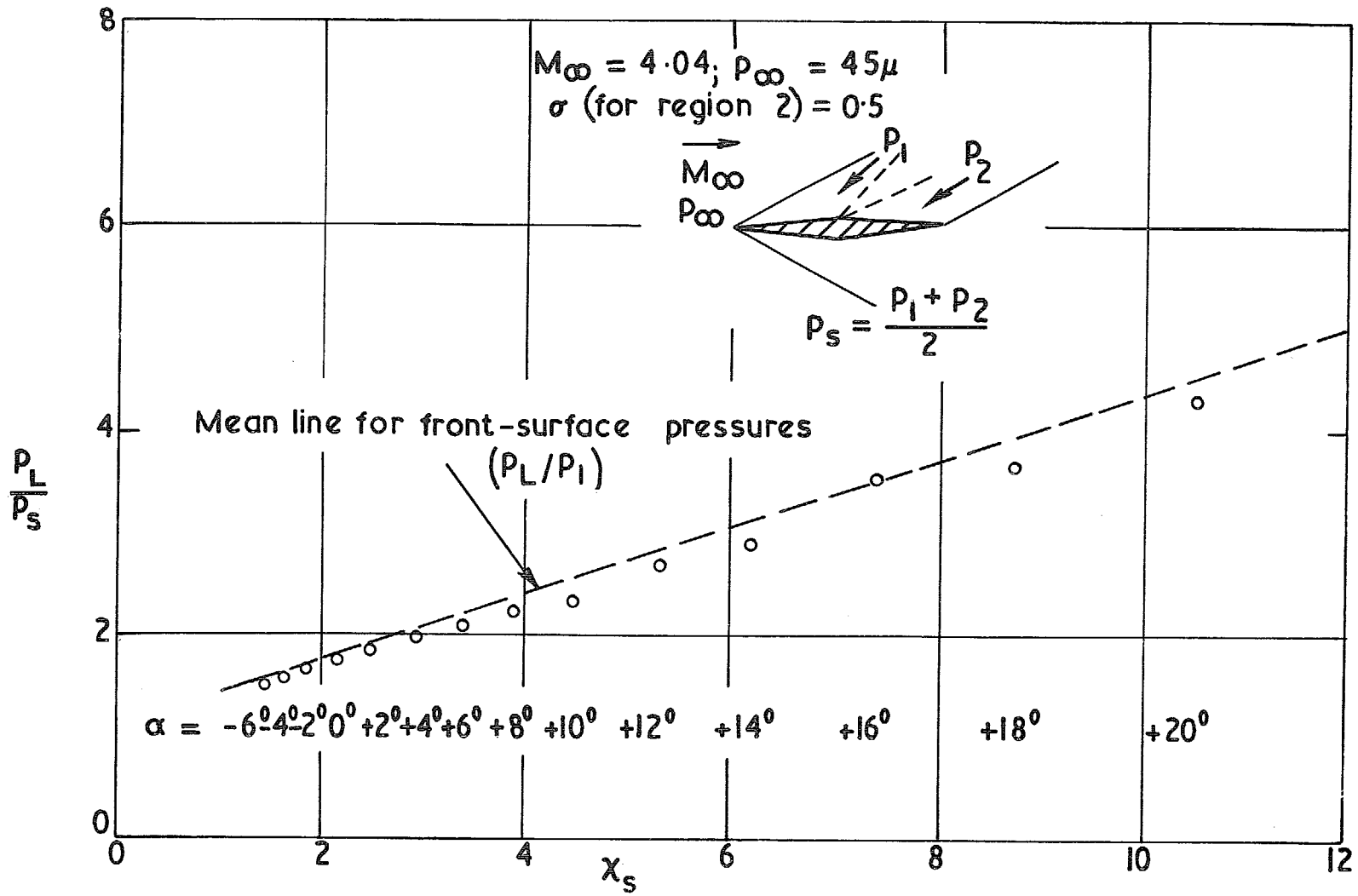

FIG. 14. Correlation of shoulder pressures on double-wedge aerofoil at $M_\infty = 4{\cdot}04$.

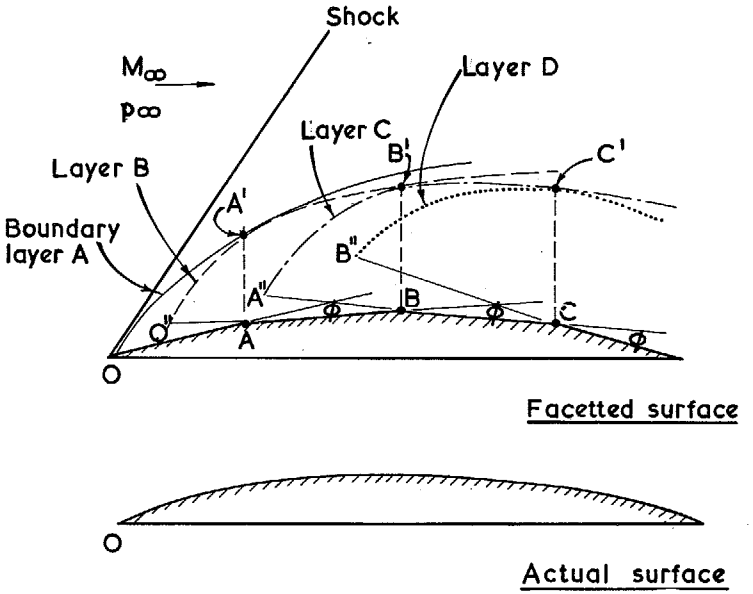

Each facet has its own equivalent boundary layer, A to D growing from an effective origin O, O", A", B". Boundary-layer thickness and slope are matched at points A', B', C'.

FIG. 15. Model of boundary-layer flow about biconvex section.

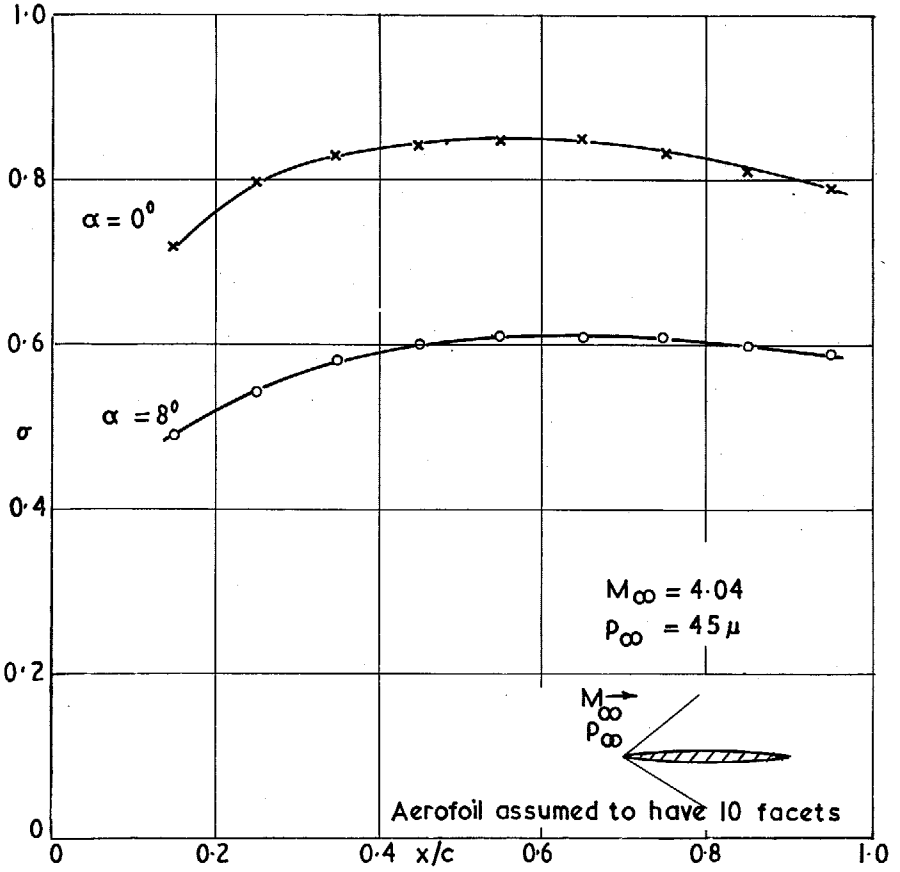

FIG. 16. Calculation of σ along surface of 'segmented' biconvex aerofoil.

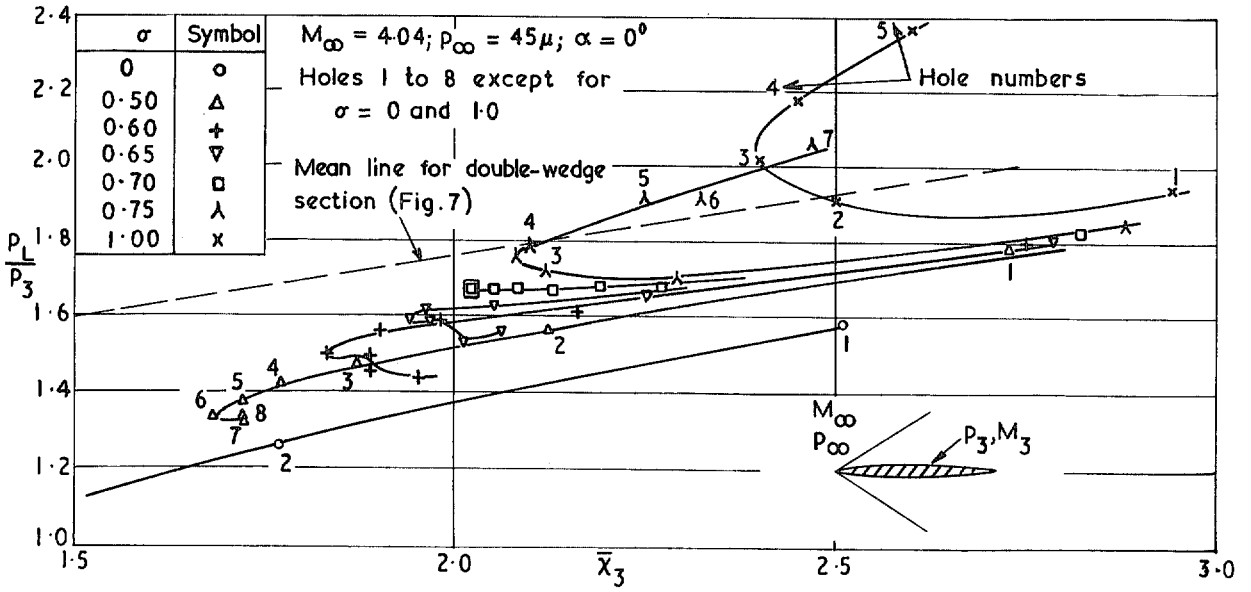

FIG. 17. Effect of σ on surface-pressure correlation on biconvex aerofoil ($M_\infty = 4{\cdot}04$).

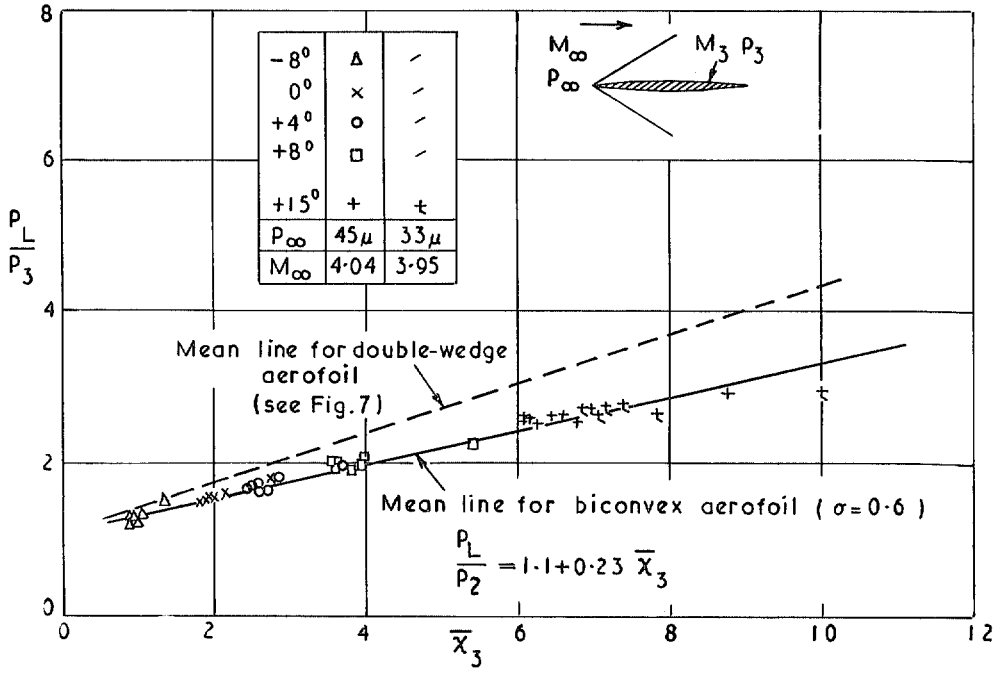

FIG. 18. Correlation of surface pressures on biconvex aerofoil over range of incidence ($\sigma = 0{\cdot}6$).

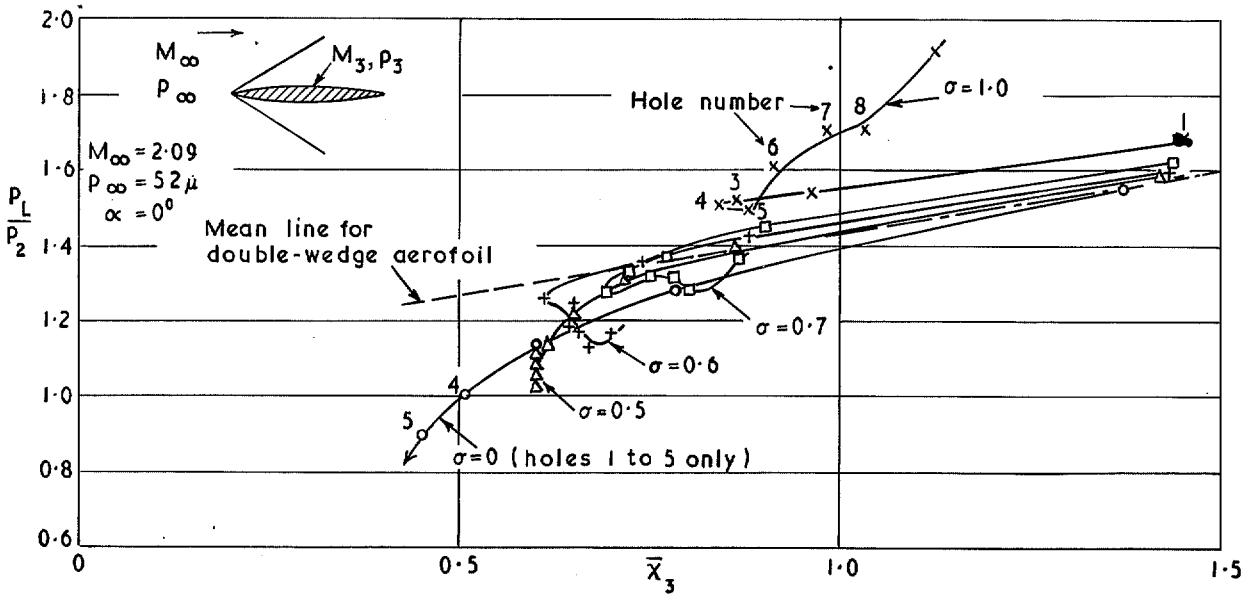

FIG. 19. Effect of σ on surface-pressure correlation for biconvex aerofoil ($M_\infty = 2{\cdot}09$).

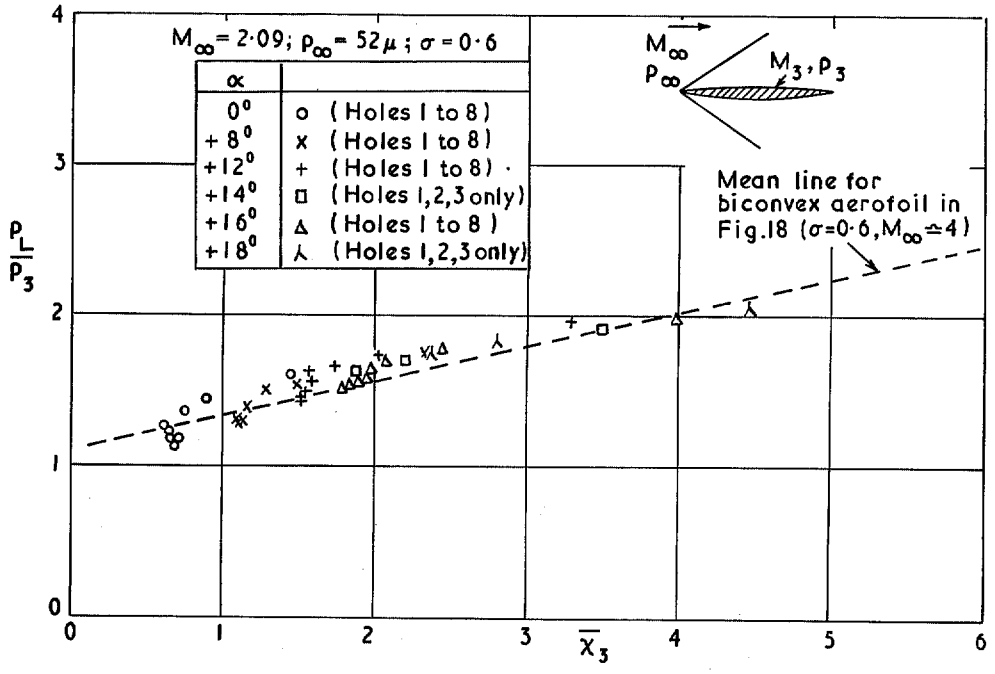

FIG. 20. Correlation of surface pressures on biconvex aerofoil for $M_\infty = 2{\cdot}09$ ($\sigma = 0{\cdot}6$).

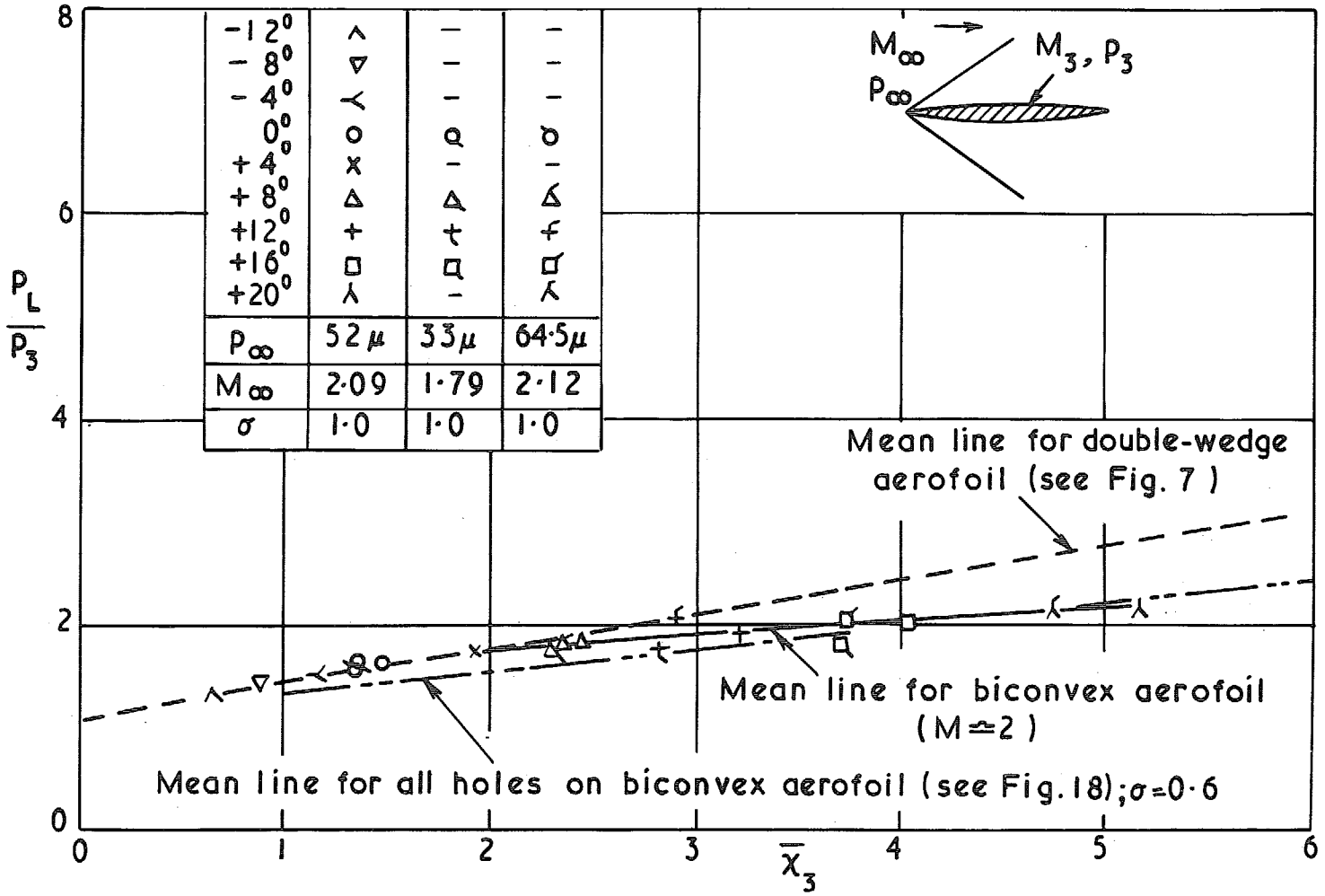

FIG. 21. Pressure correlation for $x/c = 0{\cdot}05$ on biconvex aerofoil over range of incidence at $M_\infty \simeq 2$ ($\sigma = 1{\cdot}0$).

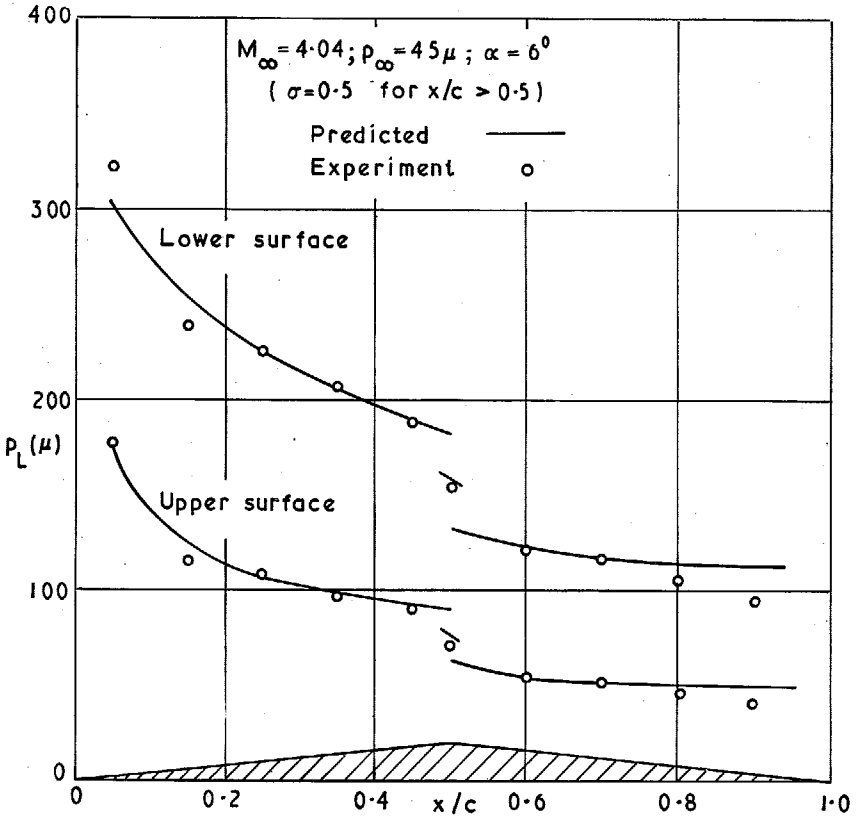

FIG. 22. Comparison of predicted and measured surface pressure distributions on double-wedge aerofoil at $\alpha = 6°$.

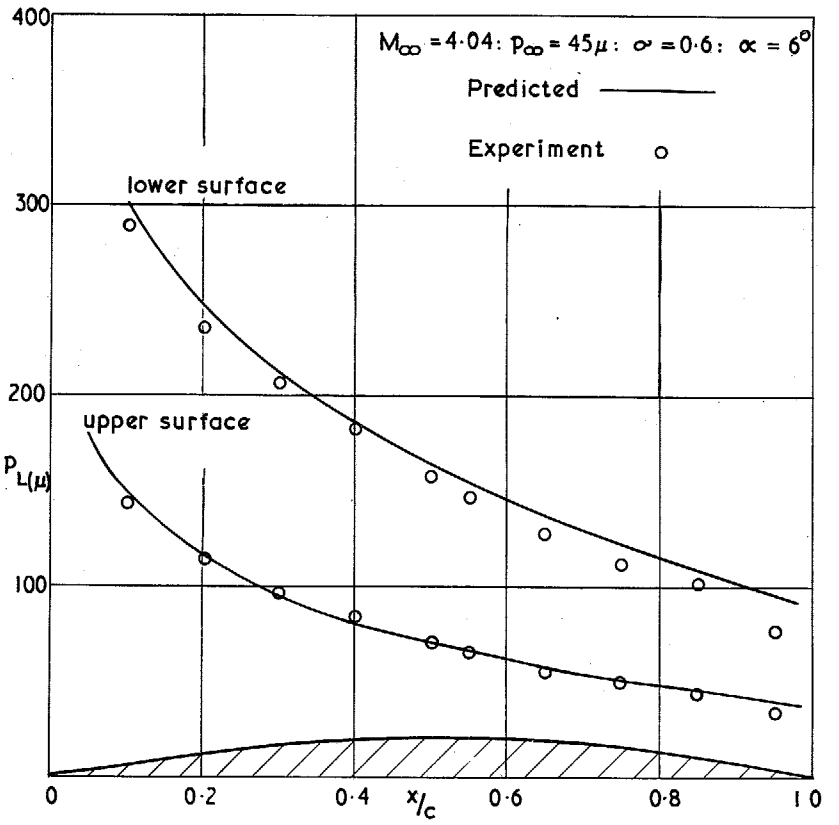

FIG. 23. Comparison of predicted and measured surface pressure distributions on biconvex aerofoil at $\alpha = 6°$.

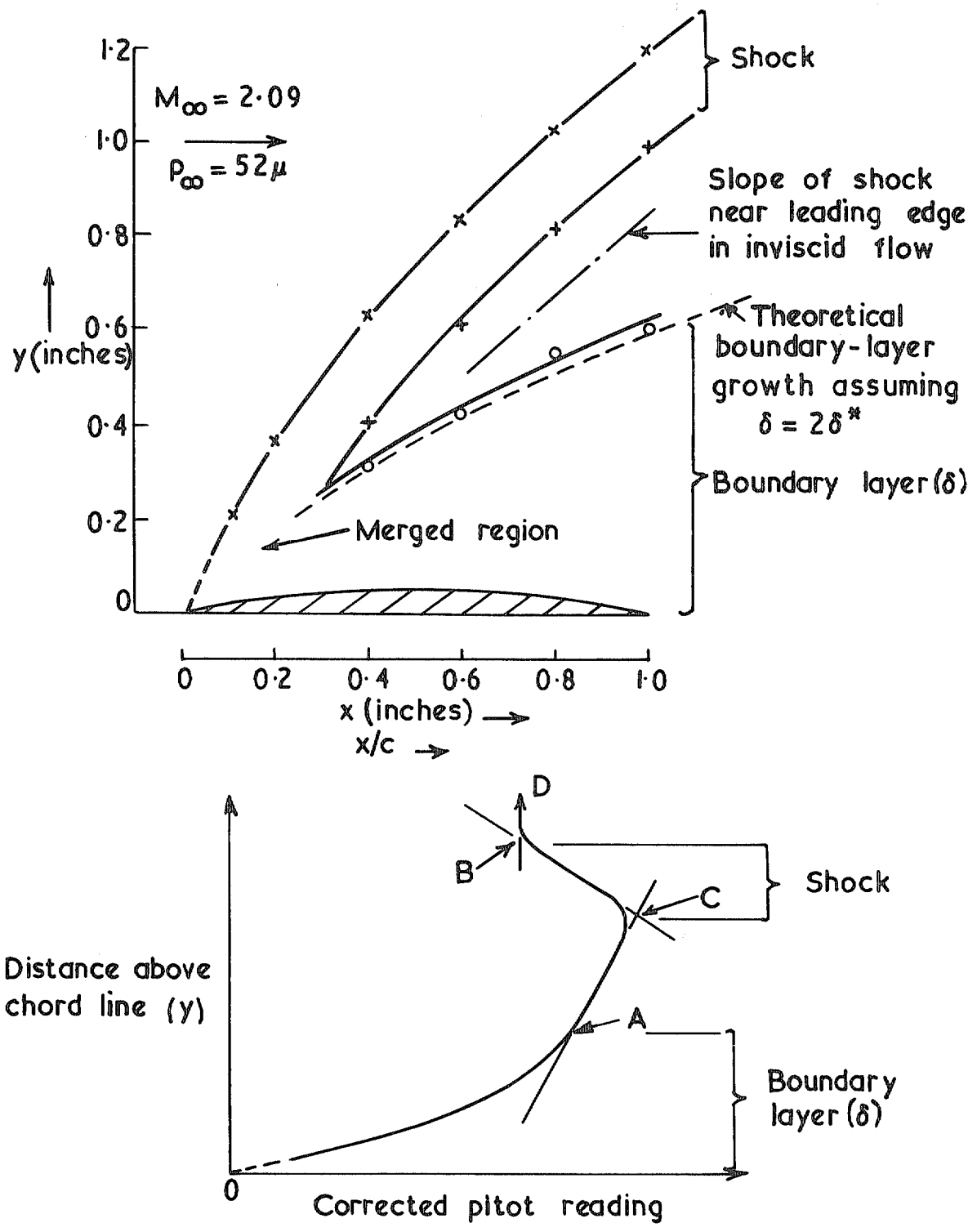

FIG. 24. Boundary layer and shock shape deduced from flow explorations at $\alpha = 0°$ (biconvex section).

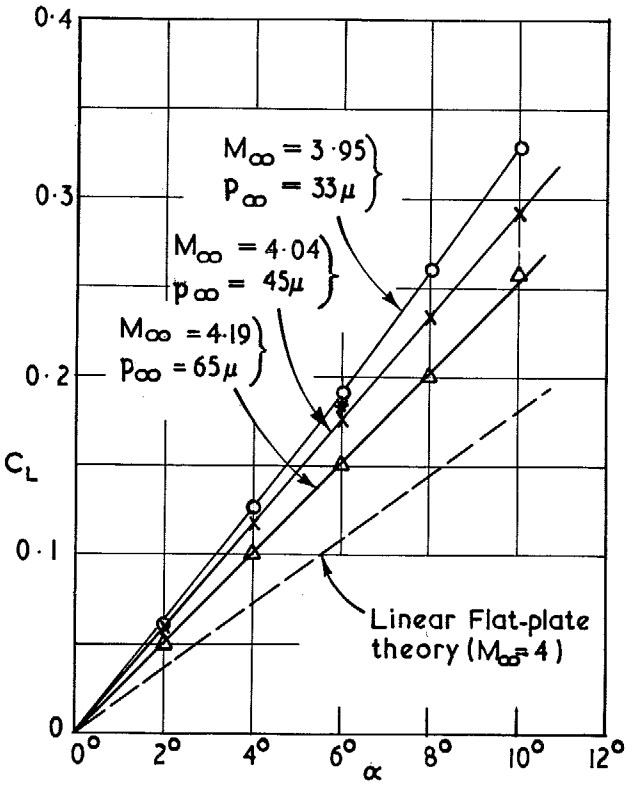

FIG. 25a. Lift-curves for biconvex aerofoil at $M_\infty \simeq 4$. (Value of C_L obtained from predicted pressure distribution of Fig. 23 at $\alpha = 6°$ shown thus $*$).

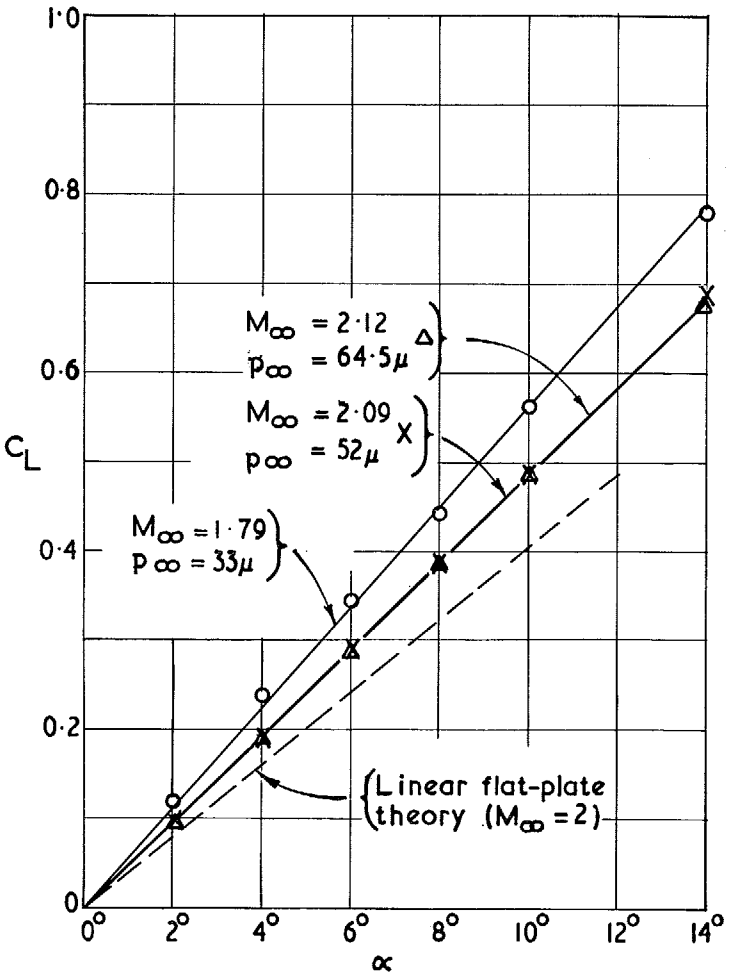

FIG. 25b. Lift curves for biconvex aerofoil at $M_\infty \simeq 2$.

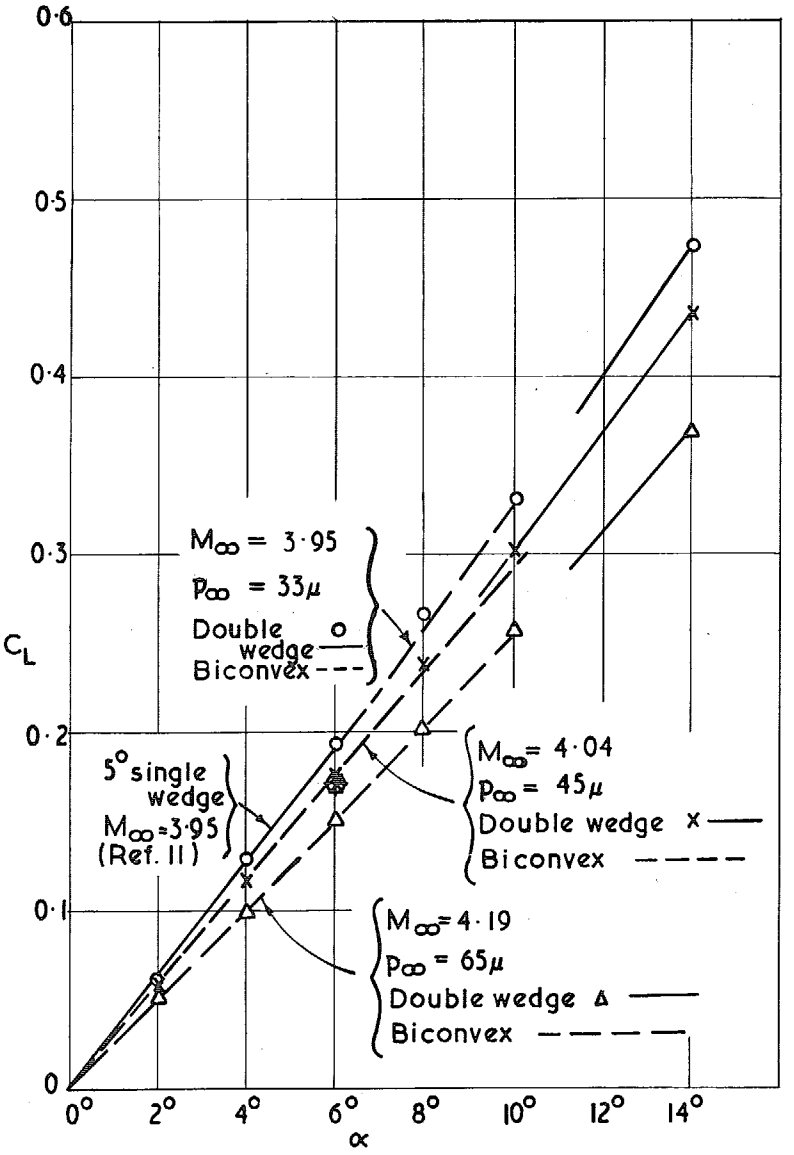

FIG. 26a. Comparison of lift results for two sections ($M_\infty \simeq 4$). (Value of C_L obtained from predicted pressure distribution of Fig. 22 at $\alpha = 6°$ shown thus $*$).

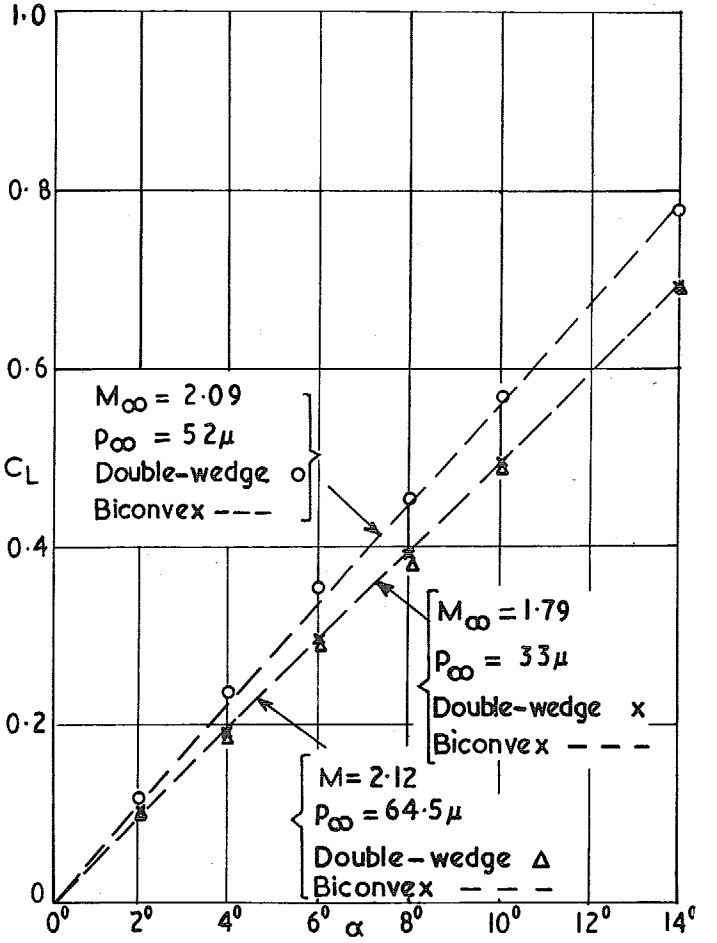

FIG. 26b. Comparison of lift results for two sections ($M_\infty \simeq 2$).

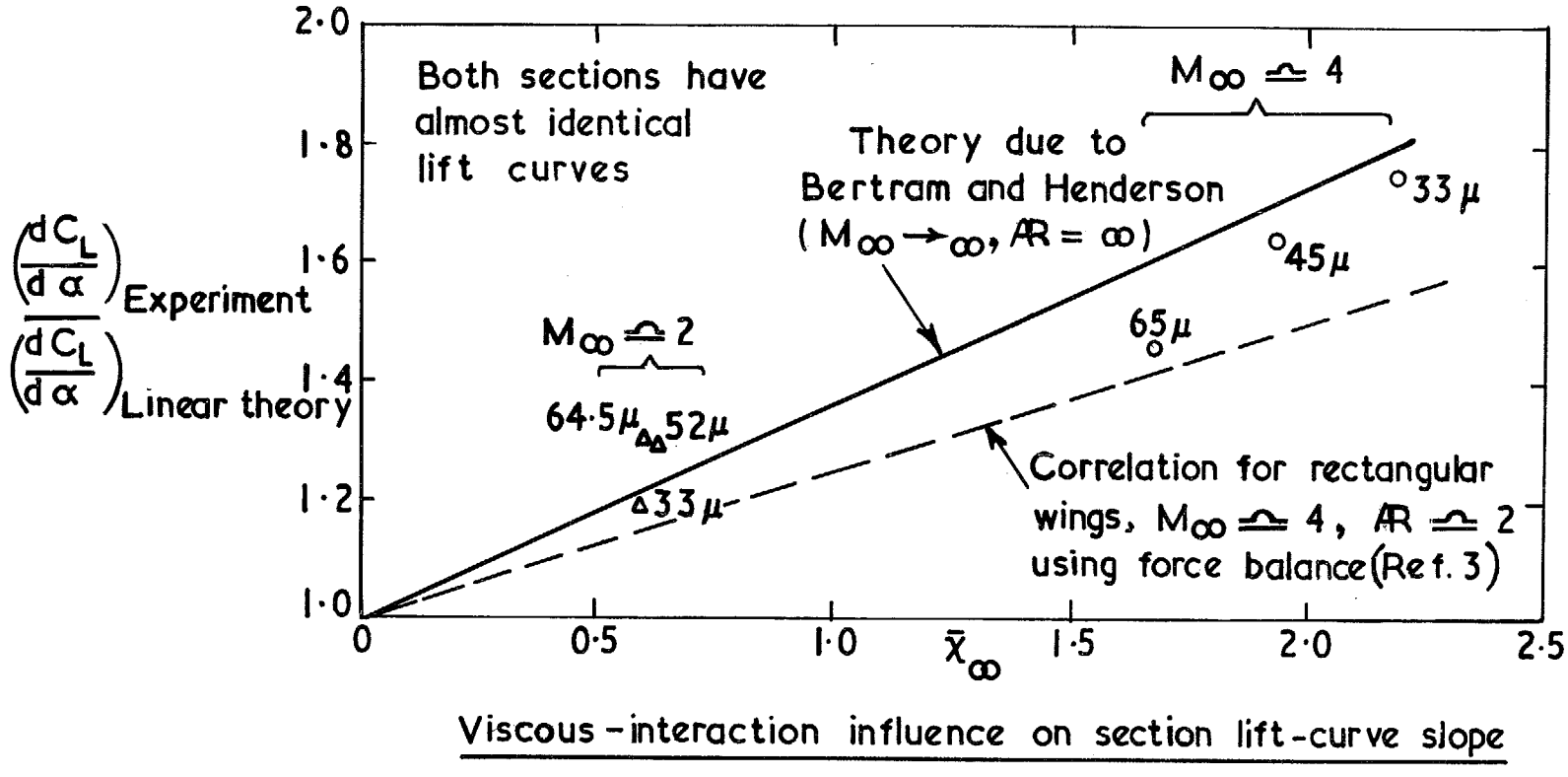

FIG. 27. Viscous-interaction influence on section lift-curve slope.

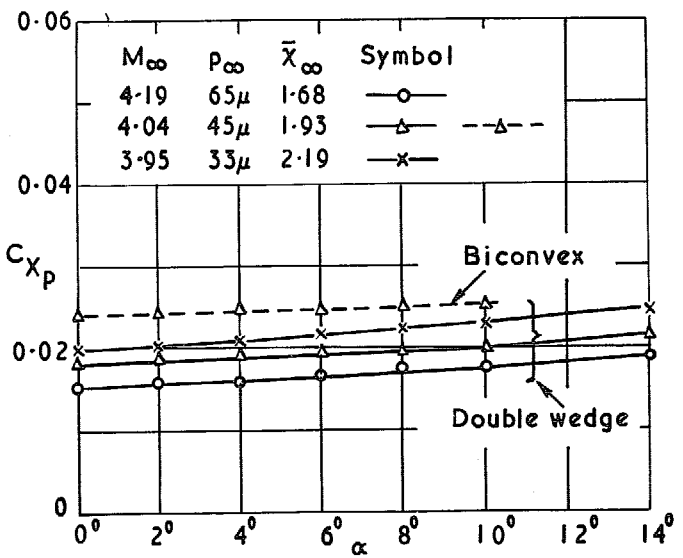

FIG. 28. Variation of axial force coefficient with incidence for $M_\infty \simeq 4$.

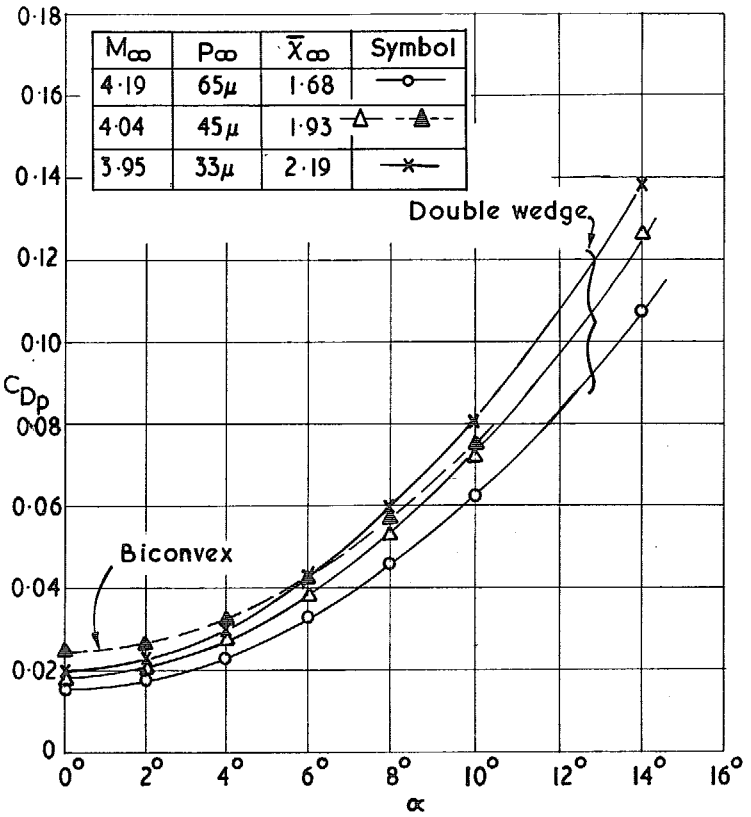

FIG. 29a. Pressure-drag curves for two sections at $M_\infty \simeq 4$.

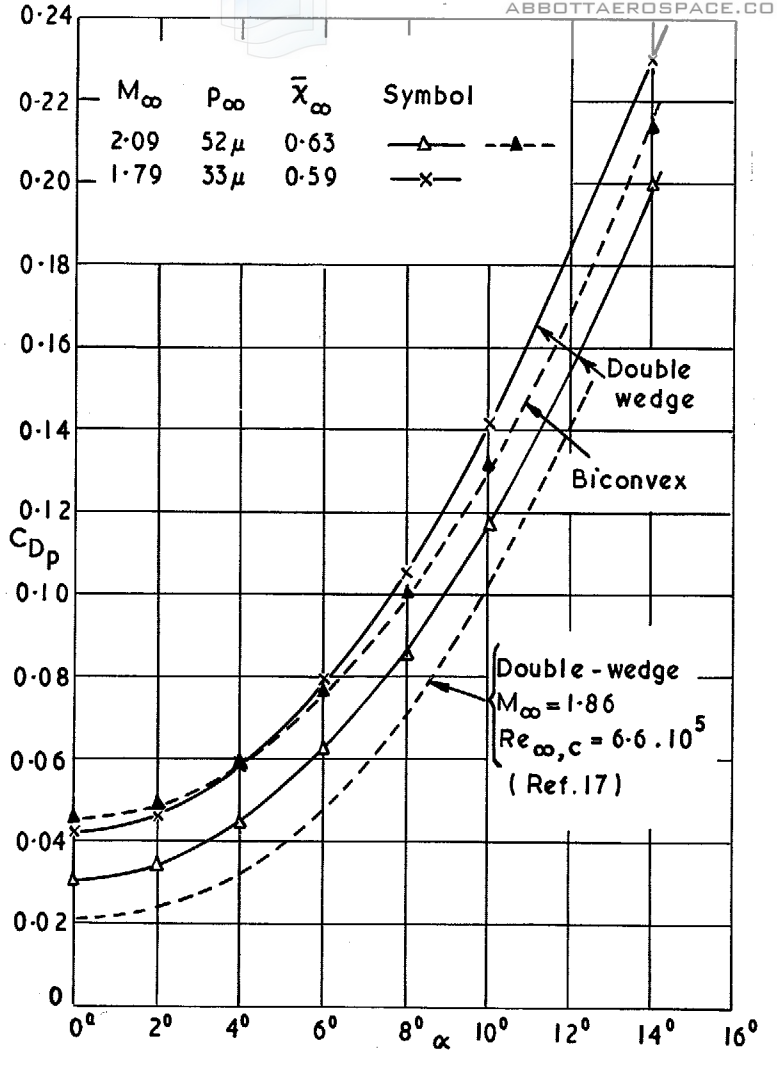

FIG. 29b. Pressure-drag curves for two sections at $M_\infty \simeq 2$.

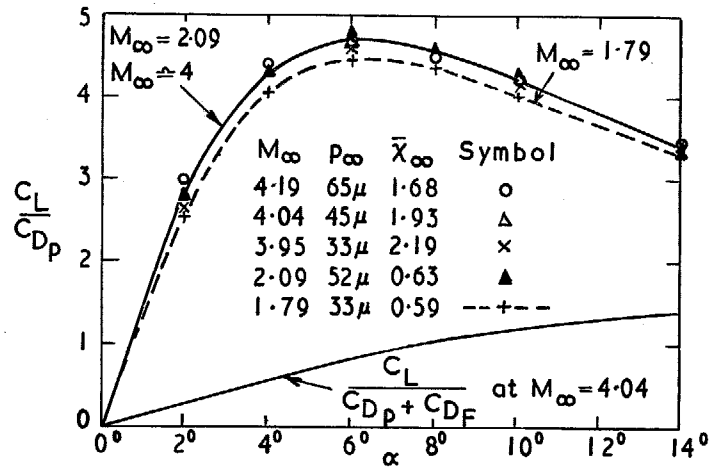

FIG. 30a. Lift/pressure-drag curves for double-wedge profile.

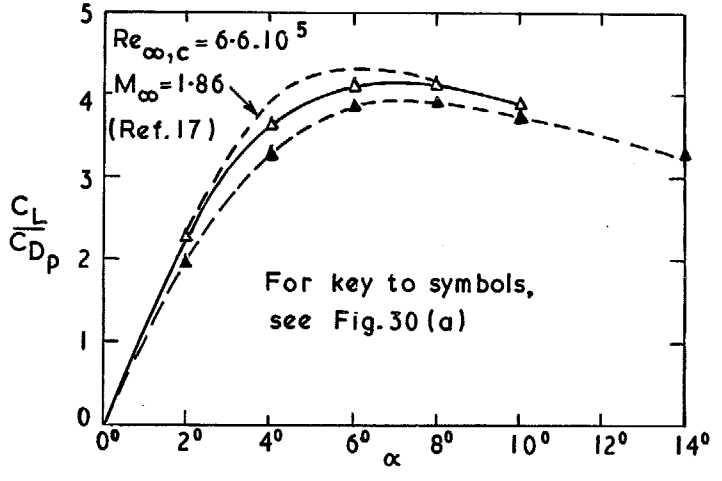

FIG. 30b. Lift/pressure-drag curves for biconvex profile.

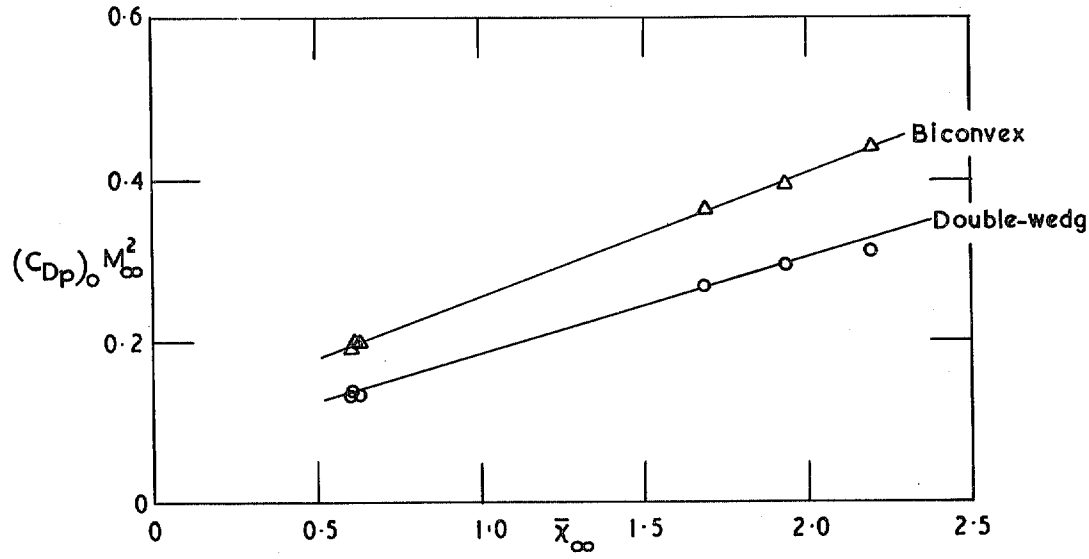

FIG. 31. Correlation of zero incidence pressure-drag results.

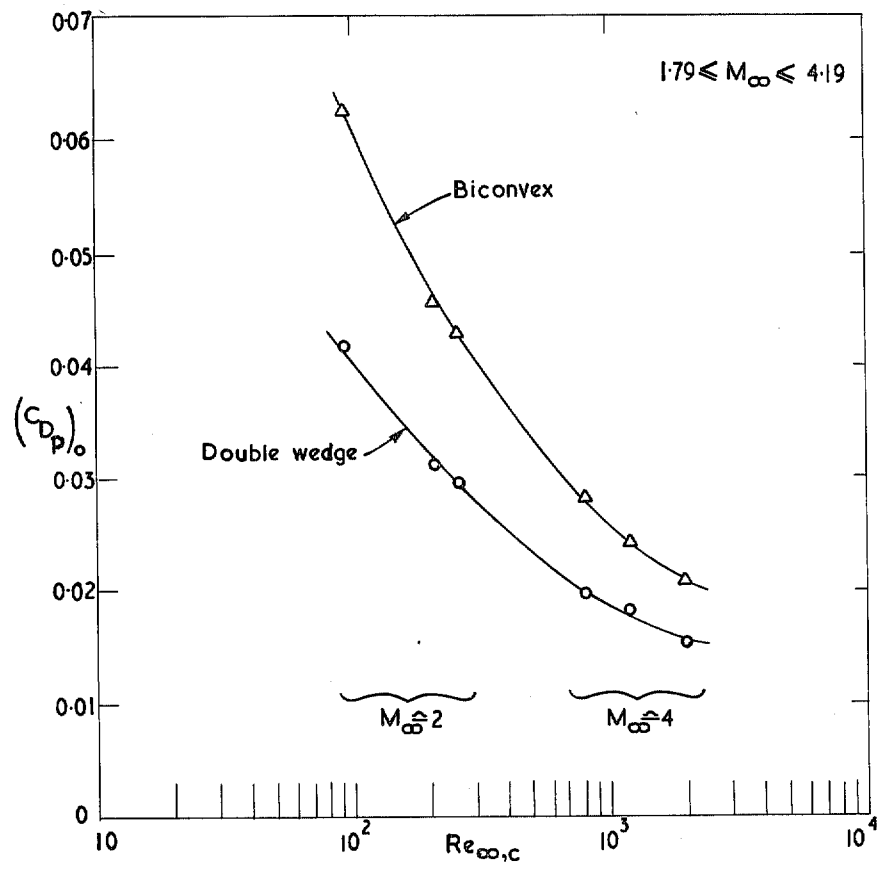

FIG. 32. Dependence of zero-incidence pressure-drag coefficient on model Reynolds number.

Printed in Wales for Her Majesty's Stationery Office by Allens Printers (Wales) Limited

Dd. 146916 K.5.

Published by
HER MAJESTY'S STATIONERY OFFICE

To be purchased from
49 High Holborn, London WC1 6HB
13a Castle Street, Edinburgh EH2 3AR
109 St. Mary Street, Cardiff CF1 1JW
Brazennose Street, Manchester M60 8AS
50 Fairfax Street, Bristol BS1 3DE
258 Broad Street, Birmingham 1
7 Linenhall Street, Belfast BT2 8AY
or through any bookseller

SBN 11 470335 3